Rheol Acta (2017) 56:387–407
DOI 10.1007/s00397-017-0994-3

ORIGINAL CONTRIBUTION

On the pulsating flow behavior of a biological fluid: human blood

Edtson Emilio Herrera-Valencia[1] · **Fausto Calderas**[2] · **Luis Medina-Torres**[3] · **Mariano Pérez-Camacho**[1] · **Leonardo Moreno**[4] · **Octavio Manero**[4]

Received: 28 August 2016 / Revised: 30 November 2016 / Accepted: 3 January 2017 / Published online: 28 February 2017

Abstract In this work, the rectilinear flow of a complex fluid (human blood) under a pulsating time-dependent pressure gradient is analyzed. A first approximation of the real case of blood flowing in a vein is described. The normalized pressure gradient simulates the pumping work of the heart while the flow geometry (circular tube) is assumed rigid, smooth, and cylindrical. The rheological behavior of blood with different cholesterol levels is modeled using the Bautista–Manero–Puig (BMP) constitutive equation. According to the analytical solution, a flow enhancement is predicted to first order which represents the optimum pumping work of the heart which governs the flow of blood in the entire body. This work is a contribution to the understanding of the complex rheology involved in the discontinuous pressure-driven flow of blood in the human body.

Keywords Hemorheology · Analytical solutions · Pulsatile flow · Stochastic noise · Complex fluid · BMP constitutive equation

✉ Fausto Calderas
fcalderas@ciatec.mx

[1] Facultad de Estudios Superiores Zaragoza, Universidad Nacional Autónoma de México, Batalla 5 de Mayo S/N, Ejército de Oriente, Iztapalapa, Mexico City 09230, Mexico

[2] CIATEC, A. C. Omega 201 Industrial Delta, C.P. 37545 León, Guanajuato, Mexico

[3] Facultad de Química, Universidad Nacional Autónoma de México, Mexico City 04510, Mexico

[4] Instituto de Investigación en Materiales, Universidad Nacional Autónoma de México, Mexico City 04510, Mexico

Introduction

The pulsatile pressure-gradient-driven non-Newtonian flow in a pipe is found in numerous biological cases and industrial situations. For example, blood flow in veins, enhanced oil recovery operations, polymer science (extrusion with oscillating dies), and time-dependent phenomena (thixotropy and rheopexy) have important implications in the nuclear waste, food, pharmacology, cosmetic, and battery industries.

In these flows, the liquid experiences a pulsating pressure gradient and there is no axial or transversal perturbation. One of the most interesting effects of this scheme is the flow enhancement caused by the pulsatile pressure gradient. This extra flow rate can be estimated as the difference between the two flow rates: the constant pressure flow rate Q_0 and the time-averaged pulsatile pressure flow rate $\langle Q(t) \rangle$ (Manero and Mena 1977; Manero and Walters 1980):

$$I_Q(\%) = 100\,\frac{\langle Q(t)\rangle - Q_0}{Q_0} \tag{1}$$

Several studies have demonstrated that deviations from Newtonian behavior (shear thinning) cause flow enhancement in pulsatile flow. This enhancement is proportional to the square of the amplitude of the oscillating pressure gradient, and its magnitude depends on the shape of the viscosity curve (Manero and Walters 1980; Phan-Thien 1978, 1980a, b, 1981, 1982; Phan-Thien and Dudek 1982a, b; Herrera et al. 2009; Herrera-Valencia et al. 2010; Lin et al. 2015). An important factor is the wave form of the pulsatile gradient (triangular, sinusoidal, or square) which has a strong effect on flow enhancement and power requirements (Barnes et al. 1969, 1971; De Andrade Lima and Rey 2005, 2006).

Human blood is one of the most important biological fluids. In the circulatory system, blood is forced to flow in

the veins and arteries by a periodic pressure gradient caused by the heart pump work. From a rheological point of view, the whole blood (plasma and cells) is a complex non-Newtonian fluid (Moreno et al. 2015), and its complex elasto-visco–plastic behavior (viscoelasticity, shear thinning, thixotropy) is caused by aggregation, disaggregation, deformation, orientation, and migration of the erythrocytes (Moyers-Gonzalez et al. 2008a, b, c; Owens 2008; Moyers-Gonzalez and Owens 2010).

The rheological behavior of blood is strongly affected by the cholesterol levels (Moreno et al. 2015), but other factors affect blood viscosity, such as hematocrit and glucose contents, triglycerides, blood type, and shape of red blood cells. Blood exhibits a complex rheological phenomena involving yield stresses when the cholesterol content is high enough (Apostolidis and Beris 2015; Apostoldis et al. 2016; Moreno et al. 2015). From a rheometrical point of view, blood is a challenge for experimentalists due to coagulation (blood clotting) in the presence of oxygen. In this regard, the use of anticoagulants such as heparin should be cautious to avoid the rheological and transport properties to be affected (Moreno et al. 2015). In this context, ethylenediaminetetraacetic acid (EDTA) has been widely used as an anticoagulant in blood samples for rheological characterizations (Moreno et al. 2015; Sousa et al. 2016). EDTA has been reported to have no significant effect upon the whole blood shear viscosity up to the maximum concentration recommended by the International Society of Clinical Hemorheology (Sousa et al. 2013). A recent review article reports on the current measuring techniques and advances in the field of hemorheology (Sousa et al. 2016).

From a mathematical point of view, the pulsating flow of blood has been modeled using various constitutive equations, namely: (1) Casson, (2) Quemada, (3) power-law, (4) Cross-Yasuda, (5) Owen (Del Rio et al. 1998; Anand and Rajagopal 2004; Prakash and Ogulu 2007; Moyers-Gonzalez et al. 2008a, b, c; Owens 2008; Siddiqui et al. 2009; Moyers-Gonzalez and Owens 2010). These constitutive equations have been tested in Poiseuille, oscillatory, and pulsating flows to simulate the blood flow through the cardiovascular system (Del Rio et al. 1998; Anand and Rajagopal 2004; Moyers-Gonzalez et al. 2008a, b, c; Owens 2008; Moyers-Gonzalez and Owens 2010). The relevance of computational simulations in the development of cardiovascular devices, in particular heart pump systems and heart valves, has been highlighted in several works (Anand and Rajagopal 2004), and there is a need for powerful, yet simple, models than can capture the full complex rheological response of blood over a range of flow conditions. Recent reports have studied the case of pulsatile flow of blood for different circumstances and with different restrictions. Majhi and Nair (1994) modeled pulsatile blood flow subjected to an externally imposed periodic body acceleration using the Crank–Nicholson numerical method. They considered blood as a third-order fluid. Massoudi and Phuoc (2008) modeled the pulsatile flow of blood considering the Fåhræus–Lindqvist effect, namely, the situation where the blood near the wall behaves as a Newtonian fluid and in the core as a non-Newtonian fluid. This effect causes the blood viscosity in a capillary (<0.4 mm) to decrease as a consequence of migration of red blood cells away from the capillary walls. They considered blood as a modified second-order fluid where the viscosity and the normal stress coefficients depend on the shear rate. EL-Shahed (2003) reported on numerical modeling of the pulsatile flow of blood through a stenosed porous medium in the presence of periodic body acceleration. Chen and Lu (2006) modeled numerically the non-Newtonian pulsatile blood flow in a bifurcation with a non-planar branch. They reported on non-Newtonian effects on the wall shear stress, oscillatory shear index, and flow phenomena during the pulse cycle. Prakash and Ogulu (2007) proposed a mathematical model for the pulsatile blood flow, in particular, the case of blood flowing in a small vessel in the cardiovascular system with a mild stenosis and considered heat transfer, modeled as a power-law fluid. Razavi et al. (2011) reported on the numerical simulation of the blood pulsatile flow in a stenosed carotid artery using six different rheological models (generalized power-law, modified Casson, Carreau, Carreau–Yasuda, power-law, Walburn–Schneck). According to their results, the power-law model produces higher deviations because it predicts viscosities far from Newtonian viscosities at low and high shear rates. Tian et al. (2013) studied the effect of atherosclerotic plaque size/geometry, Reynolds number, viscosity and pulsations on the fluid wall shear stress and its gradient, fluid normal stress, and flow shear rate by using a simplified model to simulate a pulsatile non-Newtonian blood flow past a stenosed artery caused by atherosclerotic plaques. Reddy et al. (2014) modeled pulsatile blood flow through a stenosed tapered artery in the presence of a catheter. Blood was modeled as a non-Newtonian complex fluid by an equation of state with coupled structural kinetics. Nandakumar et al. (2015) used a shear thickening model and reported on the effects of percentage stenosis and Reynolds (steady flow) and Womersley (pulsatile flow) numbers on the flow of blood through a two-dimensional channel with stenosis, and the results were compared with the Newtonian case. More recently, Ghasemi et al. (2016) simulated numerically the case of blood flow in coronary and femoral arteries. They considered blood as a third-order non-Newtonian fluid (viscoelastic) under periodic body acceleration and pulsatile pressure gradient. Partial differential equations were solved by quadrature and Crank–Nicholson numerical methods; both methods showed good agreement in the predictions of the velocity profiles. In all these pulsatile blood studies, blood viscosity is considered to be dependent on shear (shear thinning fluid), based on physical parameters or even rheometric data of blood of laboratory rats (Massoudi and Phuoc 2008). Moreno et al.

(2015) have reported the rheological behavior of blood, which is more complex than a simple shear thinning fluid, and found that the cholesterol content drastically modifies the rheology of blood leading to complex phenomena such as yield stress when cholesterol levels are high enough. Other authors (Brust et al. 2013; Kolbasov et al. 2016) have studied the rheological properties of blood in elongational flow which may become important in forensic studies (blood dripping and splashing patterns) or they may even lead to viscoelastic flow instabilities. The type of blood used for these studies is human blood plasma (Brust et al. 2013) and swine blood (Kolbasov et al. 2016). Moreover, different mathematical models have been employed to model blood flow (two- and third-order fluids). Here, we propose a mathematical model for blood flow using the Bautista–Manero–Puig (BMP) equation of state, which couples a codeformational Maxwell equation with a kinetic equation for breakdown of the structure (Bautista et al. 1999; Bautista and Soltero 2000; Bautista et al. 2002; Manero et al. 2002) which describes adequately the complex behavior of human blood with different cholesterol levels (Moreno et al. 2015). Furthermore, there is lack of reports dealing with analytical solutions of pulsatile flow in non-Newtonian blood fluids. In this regard, this work deals with the mathematical predictions of Poiseuille flow with oscillating pressure gradient of a complex biological liquid, using the BMP equation of state. In particular, the analysis of flow enhancement and yield stress present in the blood flow through a rigid capillary is included. This analysis aims to contribute to the understanding of blood flow in a vein or artery.

Blood samples

Samples were obtained from donors in the National Institute of Cardiology from research protocols of dyslipidemia and other metabolic disorders. Blood was extracted by venipuncture and later stored in tubes with EDTA to avoid coagulation. These samples do not possess significant differences in the hematocrit levels (the blood samples were selected for this study with a hematocrit level of 42%). Two tubes of 5 mL for each patient were collected. The first tube was used for biochemical determinations of total cholesterol and triglycerides. The second tube was kept the samples for rheological measurements which were readily performed during the first few minutes after extraction.

Theoretical part

Continuity and momentum balance equations

$$\frac{D\rho}{D\mathrm{t}} + \nabla\cdot\mathbf{V} = 0 \tag{2}$$

$$\frac{\partial}{\partial \mathrm{t}}\rho\mathbf{V} + \nabla\cdot\mathbf{T} = \rho\mathbf{g} \tag{3a}$$

$$\mathbf{T} = \rho\mathbf{V}\otimes\mathbf{V} + p(t)\mathbf{I} - \boldsymbol{\sigma} = \rho\mathbf{V}\otimes\mathbf{V} + p(1+\varepsilon \mathrm{n}(t))\mathbf{I} - \boldsymbol{\sigma} \tag{3b}$$

The first equation is the continuity equation (mass conservation), the second one is the momentum equation, and the third one involves the deviatoric stress tensor $\mathbf{T}$, which includes the pulsating pressure gradient. In these equations, ρ is the density, $\mathbf{V}$ is the velocity, $\otimes$ is the dyadic product, $D/D\mathrm{t}$ is the material time derivative, p is the thermodynamic pressure, $\mathbf{g}$ is the gravity acceleration, $n(t)$ is a stochastic function and, ε is a small parameter in the perturbation solution. Notice that the formulation in terms of Eq. (3b) is general and includes other contributions such as (1) orientation, (2) vorticity, (3) short and long interactions, (4) defects and textures, and so on.

BMP constitutive equation

This constitutive equation contains an evolution term to account for structure modification (Fredrickson 1964; Bautista et al. 1999). It is written in terms of a structural parameter $\varsigma(\mathrm{II_D})$ which depends on space and time, bounded by two characteristic viscosities: the zero strain-rate viscosity η_0 and the high strain-rate viscosity η_∞. This equation is coupled dynamically to a well-established non-linear rheological equation of state, the upper-convected Maxwell equation:

$$\boldsymbol{\sigma} + \frac{\varsigma(\mathrm{II_D})}{G_0}\overset{\nabla}{\boldsymbol{\sigma}} = \boldsymbol{\sigma} + \frac{\varsigma(\mathrm{II_D})}{G_0}\left\{\frac{\partial\boldsymbol{\sigma}}{\partial\mathrm{t}} + \mathbf{V}\cdot\nabla\boldsymbol{\sigma} - \left\{\nabla\mathbf{V}^{\mathrm{T}}\cdot\boldsymbol{\sigma} + \boldsymbol{\sigma}\cdot\nabla\mathbf{V}\right\}\right\} = 2\varsigma(\mathrm{II_D})\mathbf{D} \tag{4}$$

$$\frac{\mathrm{d}}{\mathrm{dt}}\varsigma(\mathrm{II_D}) = \frac{\varsigma(\mathrm{II_D})}{\lambda}\left(1-\frac{\varsigma(\mathrm{II_D})}{\eta_0}\right) + \frac{k\eta_\infty}{\lambda}\sigma_{\mathrm{y}}^{-2}\varsigma(\mathrm{II_D})\left(1-\frac{\varsigma(\mathrm{II_D})}{\eta_\infty}\right)\boldsymbol{\sigma}:\mathbf{D} \tag{5}$$

$$\mathbf{D} = \frac{1}{2}\left(\nabla\mathbf{V} + \nabla\mathbf{V}^{\mathrm{T}}\right);\ \mathrm{II_D} = \sqrt{2(\mathbf{D}:\mathbf{D})};\ \sigma_{\mathrm{y}} = \frac{1}{\sqrt{k\lambda/\eta_\infty}} \tag{6a–c}$$

In Eq. (4), $\boldsymbol{\sigma}$ is the viscoelastic stress tensor and the superscript ∇ is the upper-convected time derivative. In Eqs. (4 and 5), $\varsigma(II_D)$ can be interpreted a scalar parameter representing the flow-induced changes in structure with limits of $\eta 0$ (at low shear rates) and $\eta\infty$ under fast flow. It is important to note that the structural parameter $\varsigma(II_D)$, which has the same units as viscosity (Pa s), represents the level of structure in the system. This structure parameter is related to the number of entanglements, links, bonds, or clusters at time t, and it can be associated with a viscosity function (inverse fluidity) in the case of steady state and homogeneous flow. Therefore, $\varsigma\ (II_{\mathbf{D}}) = \eta(II_{\mathbf{D}})$. $\mathbf{D}$ is the rate of deformation tensor which is symmetric part of the velocity gradient tensor, $\mathbf{II_D}$ is the second invariant of the rate of deformation tensor $\mathbf{D}$, and G_0 is the elastic modulus. In Eq. (5), η_0 and η_∞ are the viscosities at zero and very high shear rates, respectively, and can be rewritten in terms of the product between the elastic moduli and the relaxation time at low and high shear rates. The structural relaxation time λ is related with the buildup mechanisms in the system after a period of deformation. The material parameter k can be interpreted as a kinetic constant, associated with the destruction processes. which in the case of blood are associated with blood cell disaggregation processes, and it is proportional to the irreversible work of structural breakdown (viscous dissipation). Furthermore, all the material properties of the simplest BMP model (η_0, η_∞, G_0, λ, k) are related to the fluid properties and can be estimated from independent rheological experiments in steady and unsteady flows. The viscosity at lower and upper shear rates (η_0, η_∞) can be estimated through experiments in steady shear flow. The Maxwell time and elastic modulus ($\eta 0/G0$, G_0) can be determined in small-amplitude oscillatory shear flow. The kinetic constant and structure time (k, λ) can be evaluated in stress relaxation and flow inception experiments, respectively (Soltero et al. 1999; Calderas et al. 2009, 2013). The BMP model was selected for this study due to its capacity of predicting non-Newtonian blood behavior (Moreno et al. 2015). Additionally, BMP predictions have been compared with experiments in complex fluids and good agreement has been found (Bautista and Soltero 2000; Bautista et al. 1999, 2002, 2007; Caram et al. 2006; Escalante et al. 2007; Herrera et al. 2009, Herrera-Valencia et al. 2010; Macias et al. 2003; Manero et al. 2002, 2007; Moreno et al. 2015; Tabatabaei et al. 2015). Analytical and numerical solutions for simple shear, pulsating, and oscillating flows are obtained with this model due to its simplicity as compared to more complex models (Giesekus 1966; Acierno et al. 1976; Giesekus 1982, 1984, 1985; De Kee and Chan Man Fong 1994; Quemada et al. 1981; Rao 2014; Sun and Kee 2001; Owens 2006; Moyers-Gonzalez et al. 2008a, b, c) including hybrid models using a White–Metzner constitutive equation coupled to an ad hoc viscosity function and Oldroyd-B viscoelastic models (Anand and Rajagopal 2004; Anand et al. 2013), respectively. Recently, Tabatabaei et al. (2015) have reported a comprehensive review paper on the different and hybrid mathematical models.

Rheological characterization

Rheological tests were performed in a controlled stress rheometer (AR-G2, TA® instruments) equipped with a double concentric cylinder fixture adapted for 5 mL samples. The concentric cylinder geometry is useful in low viscosity fluids, keeping uniform temperature and preventing evaporation (a water seal was used), and the velocity gradient in the gap is nearly constant. In the parallel plates, on the other hand, a correction is needed due to the non-homogeneous radial dependence of the shear rate. In addition, the gap in this geometry needs to be adjusted for each sample. The accuracy and reproducibility of rheological measurements can be affected by the tendency of blood cells to sediment and by sample confinement size and geometry (Moreno et al. 2015). This was minimized by performing the measurements right after extraction and avoiding the use of the cone and plate geometry (it is not recommended for suspensions due to the aspect ratio effects of the red cells and gap). All measurements were performed under increasing and decreasing steady state shear-rate protocols, i.e., each viscosity points was taken under steady state (<0.5% variation) and the time to reach steady flow varies depending on the shear rate applied but in no case was set under 1 min. The first step in all rheological tests is the applications of pre-shearing with a shear rate of $\gamma = 1\ s^{-1}$ to homogenize the proteins in the plasma and red blood cells, in a period of 1 min. Simple shear tests were performed from 1 to 30 s^{-1}. The steady state for a given applied shear stress was attained past the initial transients for each value of stress, with a waiting time enough to obtain the time-independent curve (Tropea et al. 2007).

Problem formulation

A schematic diagram of the pulsating flow is given in Fig. 1. The isothermal rectilinear blood flow under a pulsating time-dependent pressure gradient system is analyzed in a circular pipe of radius $r = a$, and axial length $z = L$. In this system, all physical quantities are defined in cylindrical coordinates (r, θ, z) with respect to the origin at the pipe center. In Eq. (3), the parameter ε is a small perturbation parameter, i.e., $\varepsilon << 1$. The velocity field in the capillary flow is given by $\mathbf{V} = [0, 0, Vz\ (r, t)]$, and the shear stress tensor $\boldsymbol{\sigma}$, velocity gradient $\nabla\mathbf{V}$, and shear

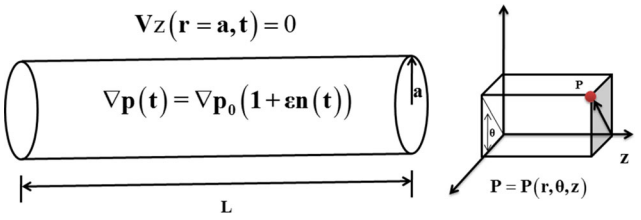

Fig. 1 Schematic representation of the flow system. A pulsating pressure gradient drives the flow along the velocity direction (z)

strain tensors $\mathbf{D} = (\nabla\mathbf{V} + \nabla\mathbf{V}^{T})/2$ are given in the following matrix form:

$$\boldsymbol{\sigma} = \begin{pmatrix} \sigma_{rr} & 0 & \sigma_{rz} \\ 0 & \sigma_{\theta\theta} & 0 \\ \sigma_{zr} & 0 & \sigma_{zz} \end{pmatrix}; \quad 2\mathbf{D} = \gamma_{rz} \begin{pmatrix} 0 & 0 & 1 \\ 0 & 0 & 0 \\ 1 & 0 & 0 \end{pmatrix} \quad (7a, b)$$

Boundary conditions are the non-slip condition at the wall $Vz(r=a,t)=0$ and the symmetry of the velocity $\partial Vz(0,t)/\partial r=0$.

Dimensionless variables, groups, and equations

Non-dimensional variables

To simplify the momentum and constitutive equations, the following dimensionless variables are introduced for the axial velocity, pressure gradient, time, shear stress, shear rate, radial coordinate, viscosity function, and frequency, respectively.

$$Vz^{*} = \frac{Vz}{Vc}; \quad p = \frac{dp}{dz}\Big/\frac{p_c}{a}; t^{*} = \frac{t}{t_c}; \sigma^{*}_{(rz)} = \frac{\sigma_{(rz)}}{\eta_0/t_c}; Q^{*} = \frac{Q}{\pi a^3/t_c}; \dot{\gamma}^{*}_{rz} = t_c\,\dot{\gamma}_{rz}$$
$$N^{*}_{(1)} = \frac{N_1}{Nc} = \frac{\sigma_{rr}-\sigma_{\theta\theta}}{Nc}; N^{*}_{(2)} = \frac{N_2}{Nc} = \frac{\sigma_{\theta\theta}-\sigma_{zz}}{Nc}; r^{*} = \frac{r}{r_c}; \varsigma^{*} = \frac{\varsigma}{\varsigma_0}; \eta^{*} = \frac{\eta}{\eta_0} \quad (8a–j)$$

To analyze the kinetic, structural, and viscoelastic mechanisms, a characteristic time t_c is defined as the inverse of the characteristic shear strain in the system $t_c = a/\langle Vz\rangle$, Nc is the characteristic normal stress difference given by $Nc=\eta_0/tc$ and rc is the characteristic dimensionless radial lenght. This timescale selection enables a comparison with other characteristic times associated to a given physical mechanism (structural $t_c = a/\langle Vz\rangle$, viscoelastic, $\lambda_0=\eta_0 G_0^{-1}$, $\lambda_\infty=\eta_\infty G_0^{-1}$, and rupture times at low and high shear rate $t_{r0}=k\eta_0$; $t_{r\infty}=k\eta_\infty$, respectively).

Non-dimensional groups

Using the previous expressions, the dimensionless components of the momentum and constitutive equations are obtained. In addition, the following dimensionless groups are defined. The first one is the dimensionless number B, defined as

$$B = \frac{\eta_0}{\eta_\infty} = \frac{\lambda_0}{\lambda_\infty} = \frac{\text{structural points at zero shear rate}}{\text{structural points at infinite shear rate}} \quad (9)$$

which is the ratio of the viscosities at low and high shear rates. Fluids may be shear thinning ($B > 1$) or shear thickening ($B < 1$). The second one is the dimensionless number $A_0 = k\eta_0/\lambda$, which is a ratio between two timescales (the rupture time at low shear rate and the structure time). When the dimensionless number A_0 is larger than one, the fluid structure recovers faster than the rupture caused by the flow (Bautista et al. 1999). It was shown that when the structural time is larger than the Maxwell time, thixotropic loops are predicted, since the structure of the fluid does not recover during the deformation period, i.e., destruction of the structure is faster than recovery (Bautista et al. 1999). One relevant case is when the kinetic constant is equal to inverse of the elastic modulus ($k = 1/G_0$). In this case, the Deborah number De_0 can be identified with the dimensionless number A_0.

$$A_0 = \frac{\eta_0\left(\langle Vz\rangle/a\right)^2}{1/k\lambda} = \frac{\text{viscous irreversible work}}{\text{kinetic structural irreversible work}} \quad (10a)$$

Reynolds and Weissenberg numbers

$$We_0 = \frac{\eta_0/G_0}{a/\langle Vz\rangle} = \frac{\text{viscoelastic mechanisms}}{\text{process mechanisms}}; \quad (10b, c)$$

$$Re_0 = \frac{\rho\langle Vz\rangle a}{\eta_0} = \frac{\text{inertial mechanisms}}{\text{viscous mechanisms}}$$

The third group is the Weissenberg number (We_0), which represents the ratio between a characteristic time (Maxwell relaxation time which is associated to the viscoelastic properties of the fluid $\lambda_0=\eta_0 G_0^{-1}$) and the characteristic buildup time. When $We_0 << 1$, the viscous component dominates over the elastic one. On the other hand, when $We_0 >> 1$, the opposite behavior is observed (elastic). Finally, the fourth group is the Reynolds number Re which relates the inertial and viscous forces in the fluid. To analyze the effect of the three characteristics numbers written in term of the viscosity at high shear rate η_∞, the following dimensionless numbers are defined:

$$A_\infty = B^{-1}A_0 = \frac{\eta_\infty(\langle Vz\rangle/a)^2}{1/k\lambda}; Re_\infty = B^{-1}Re_0$$
$$= \frac{\rho\langle Vz\rangle a}{\eta_\infty}; We_\infty = B^{-1}We_0 = \frac{\eta_\infty/G_0}{a/\langle Vz\rangle} \quad (11a)$$

Here, the dynamics of the system can be described with two dimensionless groups given by $\{Re_0 = B\,Re_\infty, A_0 = B\,A_\infty\}$ which form a material parametric space where the structural, viscous, and elastic mechanisms play an important role in the description of the Poiseuille pulsating flow. The various

combinations used to study the effect of these dimensionless groups are described in Fig. 2.

Bingham number

The Bingham number is the ratio of the yield stress and wall stress.

$$\mathrm{B_i} = \frac{\sigma_y^*}{\sigma_{w\infty}^*} = \frac{1/\sqrt{A_\infty}}{\sigma_{w\infty}^*} = \frac{\text{yield stress mechanisms}}{\text{wall stress mechanisms}}$$
$$= \begin{cases} 0 = \mathrm{B_i}; \text{fluid} \\ 0 < \mathrm{B_i} < 1; \text{fluid–solid} \\ \mathrm{B_i} = 1; \text{solid} \\ \mathrm{B_i} > 1 \ ; \text{yield stress} \end{cases} \quad (11b)$$

When the yield stress is larger than the applied wall stress, $\mathrm{B_i} \in [1, \infty)$, the system does not flow, and it flows otherwise. The map of different combinations to study the effect of the Bingham number ($\mathrm{B_i}$) on the yield stress is described in Fig. 3.

Usual parameters of the BMP model for a model-structured fluid (wormlike micellar solution) are summarized in Table 1 (for reference only).

Non-dimensional momentum equation

The non-dimensional momentum equation is

$$\mathrm{Re_0}\frac{\partial \mathrm{Vz}^*(r^*,t^*)}{\partial t^*} = -\nabla z^* p_0^*(1+\varepsilon n(t^*)) + \frac{1}{r^*}\frac{\partial}{\partial r^*}\left(r^*\sigma_{(rz)0}^*(r^*,t^*)\right) \quad (12)$$

The dimensionless boundary conditions are the (1) non-slip condition and (2) the symmetry of the flow, respectively.

$$\mathrm{Vz}^*(r^*=1,t^*) = 0 \text{ and } \dot\gamma_{rz}^*(0,t^*) = \partial \mathrm{Vz}^*(r^*,t^*)/\partial r^*\big|_{r^*=0} = 0 \quad (13a,b)$$

Non-dimensional components of the BMP equations

The relevant components of the BMP equation in non-dimensional form are given by the following coupled partial non-linear differential equations:

$$\left(1+\mathrm{We_0}\eta_0^*\left(\dot\gamma_{rz}^*\right)\frac{\partial}{\partial t^*}\right)\sigma_{(rz)0}^* - \mathrm{We_0}\sigma_{(rz)0}^* N_{(2)0}^* = \eta_0^*\left(\dot\gamma_{rz}^*\right)\dot\gamma_{rz}^* \quad (14)$$

$$\frac{d}{dt^*}\eta_0^*\left(\dot\gamma_{rz}^*\right) = \eta_0^*\left(\dot\gamma_{rz}^*\right)\left(1-\eta_0^*\left(\dot\gamma_{rz}^*\right)\right) + A_0\eta_0^*\left(\dot\gamma_{rz}^*\right)\left(1-B\eta_0^*\left(\dot\gamma_{rz}^*\right)\right)\sigma_{(rz)0}^*\dot\gamma_{rz}^* \quad (15)$$

The second normal stress difference is considered negligible, and the first one is decoupled from the set of equations; hence, $\mathrm{We_0}\eta_0^*\left(\dot\gamma_{rz}^*\right)N_{(2)0}^* \cong 0$.

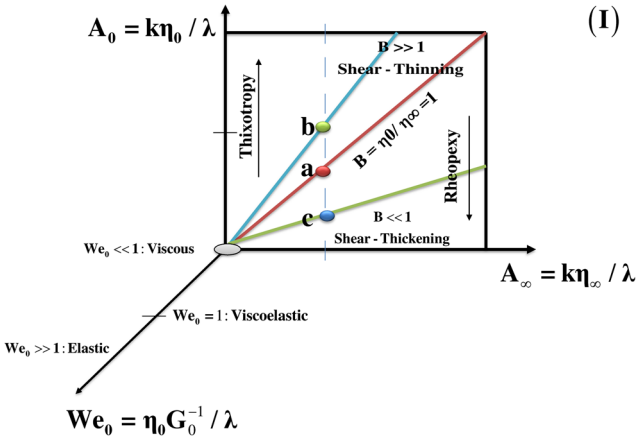

Fig. 2 Map showing the different combination of the proposed dimensionless groups (A_0, A_∞, $\mathrm{We_0}$, B)

Dimensionless flow rate

Integrating by parts, the flow rate can be expressed in the following form:

$$Q^*(t^*) = \int_0^{2\pi}\int_0^1 \mathrm{Vz}^*(r^*,t^*)r^*dr^*d\theta = \pi\mathrm{Vz}^*(r^*=1,t^*) - \pi\int_0^1\left(\dot\gamma_{(rz)}^*\right)r^{*2}dr^* \quad (16a)$$

Integration of Eq. (16a) gives the flow rate:

$$Q^* = \int_0^1\left(-\dot\gamma_{(rz)}^*\right)r^{*2}dr^* = \frac{1}{3}\left(-\dot\gamma_{(rz)}^*\right)_{r^*=1} + \frac{1}{3}\times\int_0^{\dot\gamma_{(rz)}^*|_{r^*=1}} r^{*3}d\dot\gamma_{(rz)}^*$$
$$= \frac{1}{3}\dot\gamma_w^* + \frac{1}{3}\int_0^{-\dot\gamma_w^*} r^{*3}d\dot\gamma_{(rz)}^* \quad (16b)$$

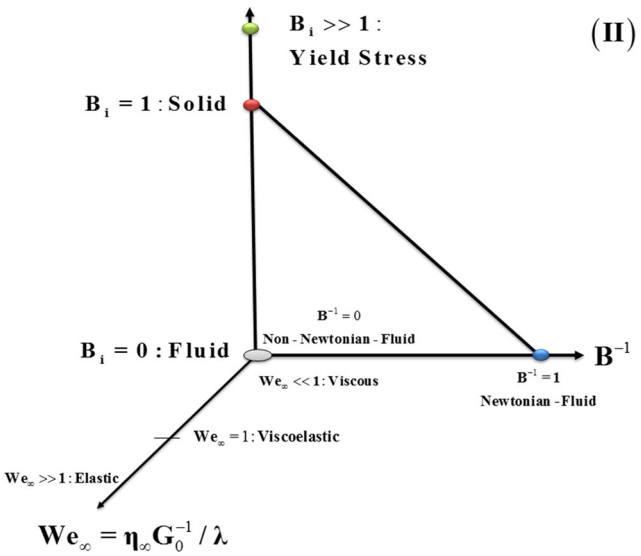

Fig. 3 Map showing the different combinations of the proposed dimensionless groups ($\mathrm{We_\infty}$, B^{-1}, $\mathrm{B_i}$) to characterize the yield stress of blood

Table 1 Material parameters values of the BMP equation of a wormlike micellar solution

BMP rheological equation	Kinetic constant	Restructuration time	Elastic moduli	Viscosity at low shear rate	Viscosity at high shear rate
Material properties	$k \times 10^6$ [Pa^{-1}]	λ [s]	G_0 [Pa]	$\varphi_0 = 1/\eta_0$ [Pa^{-1} s^{-1}]	$\varphi_\infty = 1/\eta_\infty$ [Pa^{-1} s^{-1}]
Shear thickening	39	0.14	185	0.0053	0.0002, 0.002
Shear thinning	39	0.14	185	0.0053	0.20, 1
Newtonian	39	0.14	185	0.0053	0.0053
Yield stress	39	0.14	185	0, 0.001, 0.001, 0.0053, 1, 10.5	10.5
Thixotropy	39	0.14, 0.10, 0.01, 0.001	185	0.0053	1

In Eq. (16a), the non-slip condition at wall pipe/capillary was used: $Vz^*(r^* = 1, t^*) = 0$. Equations 16a and 16b give the volumetric flow as a function of the wall stress and wall shear strain, respectively.

Stochastic non-dimensional function

A non-dimensional stochastic function $n(t^*)$ is considered, and the pulsating flow equation is given in the non-dimensional form (Eq. 12). It is assumed that the pulsating pressure gradient is represented by a stochastic function $n(t)$. This function represents random pulsatile oscillations of small amplitude. Analytical progress is possible if $n(t^*)$ is considered as a stationary random function of time (Phan-Thien 1978, 1980a, b, 1981, 1982; Phan-Thien and Dudek 1982a, b; Herrera et al. 2009; Herrera-Valencia et al. 2010). The perturbation parameter ε is small (<<1) and represents the amplitude of the perturbation solution which is only valid for small amplitudes.

$$n(t^*) = \int_{-\infty}^{+\infty} \mathrm{Exp}(i\alpha t^*)\,dZ(\alpha);\quad R(s)$$

$$= \left\langle \overline{n(t^*)}\, n(t^* + s) \right\rangle = \int_{-\infty}^{+\infty} \mathrm{Exp}(i\alpha s)\Omega(s)\,d\alpha \qquad (17a, b)$$

where $dZ(\alpha)$ is an interval random function of α with zero mean and uncorrelated increments

$$\langle dZ(\alpha)\rangle = 0;\ \left\langle dZ(\alpha_i)\overline{dZ}(\alpha_j)\right\rangle$$

$$= \delta_{ij}\Omega(\alpha_i)d\alpha_j;\ \Omega(s)$$

$$= \frac{1}{2\pi}\int_{-\infty}^{+\infty} \mathrm{Exp}(-i\alpha s)R(s)\,d\alpha \qquad (18a–c)$$

In Eqs. (17) and (18), $\langle\rangle$ denotes an ensemble average and the overbar a complex conjugate quantity, δ_{ij} is the Kronecker delta and $\Omega(s)$ is the spectral density of $n(t^*)$. The absolute value of $R(s)$, i.e., $|R(s)|$ tends to zero fast enough as the absolute value of s goes to infinity ($|s| \to \infty$), a condition met by most, if not all, physically realizable processes. Particular stochastic functions have been suggested (Phan-Thien 1978, 1980a, b, 1981; Phan-Thien 1981; De Andrade Lima and Rey 2005; De Andrade Lima and Rey 2006). The simplest expressions do not consider the effect of the harmonic contributions. Other approaches have considered the effect of the harmonics through Fourier expansions with different mathematical functions (Phan-Thien 1978, 1980a, b, 1981, 1982). In this work, no particular stochastic function is considered, since the approach considered here is more general and it states that for any particular physical noise, the Weinner–Kitchen formalism is used (Phan-Thien 1978, 1980a, b, 1981, 1982).

Perturbation scheme

Analytical expressions for the flow enhancement and power requirements require a quasi-static perturbation solution in terms of a small parameter (Barnes et al. 1969, 1971; Manero and Mena 1977; Davies et al. 1978; Phan-Thien 1978; Mena et al. 1979; Manero and Walters 1980; Phan-Thien 1980a, b, 1981; Phan-Thien and Dudek 1982a, 1982b; Herrera et al. 2009; Herrera-Valencia et al. 2010). The dimensionless shear strain can be expressed in a power series of the parameter ε:

$$\dot{\gamma}^*_{rz}(r^*, t^*) = \varepsilon^0 \dot{\gamma}^*_{(rz)0}(r^*) + \varepsilon^1 \dot{\gamma}^*_{(rz)1}(r^*, t^*) + O(\varepsilon^2) \qquad (19)$$

The dimensionless shear viscosity, stress, and flow rate can be expressed in power series of ε (provided that $\varepsilon << 1$):

$$\eta^*(r^*, t^*) = \varepsilon^0 \eta^*_0(r^*) + \underbrace{\varepsilon^1 \dot{\gamma}^*_{(rz)1}(r^*, t^*)\dot{\eta}^*_0(r^*)}_{\eta^*_1(r^*, t^*)} + O(\varepsilon^2) \qquad (20)$$

$$\sigma^*_{(rz)}(r^*, t^*) = \varepsilon^0 \sigma^*_{(rz)0}(r^*) + \underbrace{\varepsilon^1 \dot{\gamma}^*_{(rz)1}(r^*, t^*)\dot{\sigma}^*_{(rz)0}(r^*)}_{\sigma^*_{(rz)1}(r^*, t^*)} + O(\varepsilon^2) \qquad (21)$$

Integrating Eq. (19) with respect to the cross section area, the flow rate expansion is obtained:

$$Q^*(t^*) = -\int_0^1 \dot{\gamma}^*_{rz}(r^*,t^*)r^{*2}dr^* = \varepsilon^0\left(-\int_0^1 \dot{\gamma}^*_{(rz)0}(r^*)r^{*2}dr^*\right) + \varepsilon^1\left(-\int_0^1 \dot{\gamma}^*_{(rz)1}(r^*,t^*)r^{*2}dr^*\right) + O(\varepsilon^2) \quad (22)$$

where

$$Q^*(t^*) = \varepsilon^0 Q_0 + \varepsilon^1 Q_1(t^*) + \ldots + \varepsilon^j Q_j(t^*) \quad (23)$$

The total flow rate and the *j*th flow rate contribution are given by

$$Q^*(t^*) = -\int_0^1 \dot{\gamma}^*_{rz}(r^*,t^*)r^{*2}dr^*; Q^*_j(t^*) = -\int_0^1 \dot{\gamma}^*_{(rz)j}(r^*,t^*)r^{*2}dr^* \quad (24a, b)$$

The Taylor theorem allows expressing $\sigma^*_{(rz)j}(r^*,t^*)$ and $\eta^*_j(r^*,t^*)$ in terms of the derivatives of $\tau_0(r^*)$ and $\eta^*_0(r^*)$, wherein the shorthand notation has been used (Phan-Thien 1978, 1980a, b).

$$\dot{\sigma}^*_{(rz)0}\left(\dot{\gamma}^*_{(rz)0}\right) = \frac{d}{d\dot{\gamma}^*_{(rz)0}}\sigma^*_{(rz)0}\left(\dot{\gamma}^*_{(rz)0}\right), \dot{\eta}^*_0(r^*) = \frac{d}{d\dot{\gamma}^*_{(rz)0}}\eta^*_0(r^*) \quad (25, 26)$$

It is important to note that the particular perturbation expansions for the viscosity and the shear stress are different from other variables expansions, because it allows the decoupling of the upper-convected Maxwell equation from the kinetic equation of the BMP model. In addition, the flow enhancement can be expressed in terms of the higher derivatives of the shear stress and viscosity to zeroth order (Phan-Thien 1978, 1980a, b; Phan-Thien and Dudek 1982a, 1982b; Herrera et al. 2009; Herrera-Valencia et al. 2010). Details of the perturbation scheme used to solve the problem can be found elsewhere (Herrera et al. 2009; Herrera-Valencia et al. 2010).

Perturbation solutions

Zeroth order solution (homogeneous solution)

Substitution of Eqs. (19–21) in Eqs. (12–15) and equating terms of the same order in the perturbation parameter, leads to the zeroth order solution O (ε^0):

$$\sigma^*_{(rz)0}\left(\dot{\gamma}^*_{rz}\right) = \eta^*\left(\dot{\gamma}^*_{rz}\right)\dot{\gamma}^*_{rz} = \frac{A_0\dot{\gamma}^{*2}_{rz} - 1 + \sqrt{\left(A_0\dot{\gamma}^{*2}_{rz}-1\right)^2 + 4A_0B\dot{\gamma}^{*2}_{rz}}}{2A_0B\dot{\gamma}^{*2}_{rz}}\dot{\gamma}^*_{rz}. \quad (27)$$

Notice that Eq. (27) was obtained from the condition of steady state and homogeneous simple shear flow of the BMP constitutive equation (Manero et al. 2002). In Eq. (27), $\eta^*\left(\dot{\gamma}^*_{rz}\right)$ is the viscosity function of the BMP equation and the shear strain can be calculated from Eq. (27)

$$\dot{\gamma}^*_{rz}\left(\sigma^*_{(rz)0}\right) = \varphi^*\left(\sigma^*_{(rz)0}\right)\sigma^*_{(rz)0} = \frac{A_0B\sigma^{*2}_{(rz)0} - 1 + \sqrt{\left(A_0B\sigma^{*2}_{(rz)0}-1\right)^2 + 4A_0\sigma^{*2}_{(rz)0}}}{2A_0\sigma^{*2}_{(rz)0}}\sigma^*_{(rz)0} \quad (28)$$

Wall shear strain

At small Reynolds numbers ($Re_0 << 1$), integration with respect to the radial coordinate of the shear stress and pressure gradient gives

$$\frac{A_0\dot{\gamma}^{*2}_{rz} - 1 + \sqrt{\left(A_0\dot{\gamma}^{*2}_{rz}-1\right)^2 + 4A_0B\dot{\gamma}^{*2}_{rz}}}{2A_0B\dot{\gamma}^{*}_{rz}} = -\sigma^*_{w0}r^* \quad (29)$$

In Eq. (29), $\sigma^*_{w0} = -\sigma^*_{(rz)0}\big|_{r^*=1}$ is the wall stress and the boundary condition $\sigma^*_{(rz)0} = 0$ at $r^* = 0$ has been used. The wall shear strain is defined as the shear strain evaluated in the radial coordinate $r^* = 1$, i.e., $\dot{\gamma}^*_w = -\dot{\gamma}^*_{rz}\big|_{r^*=1}$

Flow rate

Substitution of the shear strain to zeroth order $\dot{\gamma}^*_{(rz)} = \varphi^*\left(\sigma^*_{(rz)0}\right)\sigma^*_{(rz)0}$ in the integral expression of the flow rate (Eq. 16a), the resulting expression, can be evaluated applying standards integral methods, as explained in the "Appendix." Finally, the flow rate is given by the following analytical form:

$$Q^*_{BMP}\left[A_0, B, \sigma^*_{w0}\right] = \varphi^*_0\left[A_0, B, \sigma^*_{w0}\right]\frac{\sigma^*_{w0}}{4} = \varphi^*_0\left[A_0, B, \sigma^*_{w0}\right]Q^*_N \quad (30)$$

where the dimensionless fluidity is given by

$$\varphi_0^*[A_0,B,\sigma_{w0}^*]=\frac{1}{2}B-\frac{1}{A_0\sigma_{w0}^{*2}}+\frac{1}{2A_0^2B^2\sigma_{w0}^{*4}}\left(\left(A_0B^2\sigma_{w0}^{*2}+2-B\right)\left(\sqrt{\left(A_0B\,\sigma_{w0}^{*2}-1\right)^2+4A_0\sigma_{w0}^{*2}}\right)-(2-B)\right)+\frac{2}{A_0^2\sigma_{w0}^{*4}}\left(\frac{B-1}{B^3}\right)\mathrm{Log}\left|\frac{2+A_0B^2\sigma_{w0}^{*2}+B\left(\sqrt{\left(A_0B\,\sigma_{w0}^{*2}-1\right)^2+4A_0\sigma_{w0}^{*2}}-1\right)}{2}\right| \tag{31}$$

Equation (30) represents the general expression for the dimensionless flow rate, which is obtained as the product of the Newtonian flow rate and a generalized dimensionless fluidity function (Eq. 31). This analytical function signals the departure from the Newtonian behavior through the dimensionless numbers associated to a particular mechanism (shear thinning and yield stress) in the complex system $\{A_0, B\}$. This function has the following analytical limiting values in terms of the shear thinning, kinetic, and viscous mechanisms:

$$\varphi_0^*[A_0,B,\sigma_{w0}^*]=\begin{cases}\lim_{\sigma_{w0}^*\to 0}\varphi_0^*=1\\ \lim_{A_0\to 0}\varphi_0^*=\lim_{B\to 1}\varphi_0^*=1\\ \lim_{\sigma_{w0}^*\to\infty}\varphi_0^*=\lim_{A_0\to\infty}\varphi_0^*=\begin{cases}B>>1;\text{ shear thinning}\\ B<<1;\text{ shear thickening}\end{cases}\\ \lim_{B\to 0}\varphi_0^*\to 0\end{cases} \tag{32}$$

Yield stress

The shear stress function is given by

$$\sigma_{(rz)_\infty}^*\left(\dot{\gamma}_{rz}^*\right)=\eta_\infty^*\left(\dot{\gamma}_{rz}^*\right)\dot{\gamma}_{rz}^*=\frac{\dot{\gamma}_{rz}^{*2}-A_0^{-1}+\sqrt{\left(\dot{\gamma}_{rz}^{*2}-A_0^{-1}\right)^2+4\,\sigma_y^{*2}\dot{\gamma}_{rz}^{*2}}}{2\dot{\gamma}_{rz}^{*2}}\dot{\gamma}_{rz}^* \tag{33}$$

and the shear strain $\dot{\gamma}_{rz}^*\left(\sigma_{(rz)_\infty}^*\right)=\varphi_\infty^*\left(\sigma_{(rz)_\infty}^*\right)\sigma_{(rz)_\infty}^*$

$$\dot{\gamma}_{rz}^*\left(\sigma_{(rz)_\infty}^*\right)=\sigma_y^*\frac{\left(\sigma_{(rz)_\infty}^*/\sigma_y^*\right)^2-1+\sqrt{\left(\left(\sigma_{(rz)_\infty}^*/\sigma_y^*\right)^2-1\right)^2+4B^{-1}\left(\sigma_{(rz)_\infty}^*/\sigma_y^*\right)^2}}{2\left(\sigma_{(rz)_\infty}^*/\sigma_y^*\right)^2}\left(\sigma_{(rz)_\infty}^*/\sigma_y^*\right). \tag{34}$$

The yield stress is controlled by the ratio $\left(\sigma_{(rz)_\infty}^*/\sigma_y^*\right)$. In the following section, the yield stress fluidity and flow rate are analyzed.

Shear strain vs Bingham number

The velocity profile with yield stress and flow rate are calculated using the viscosity at high shear rates η_∞ as a characteristic viscosity, since the viscosity at low shear rates diverges (fluidity tends to zero). The shear strain can be expressed as in terms of the Bingham number B_i (Eq. 11):

$$\dot{\gamma}_{(rz)}^*=-\sigma_y^*\frac{r^{*2}-B_i^2+\sqrt{\left(r^{*2}-B_i^2\right)^2+4B^{-1}B_i^2r^{*2}}}{2B_ir^*} \tag{35}$$

The dimensionless shear stress r^* can be interpreted as a reduced shear stress which is bounded from zero to unity, i.e., $r^*\in(0,1]\subset R$. When the reduced shear stress r^* is equal to one, i.e., $r^*\to B_i$, the value of the shear strain is equal to $\dot{\gamma}_{(rz)0}^*\to 1/\sqrt{B}\cong 0$. Here, the axial velocity is independent of the dimensionless radial coordinate.

Yield stress flow rate

In the yield stress case, the flow rate can be analyzed in two situations, one of them under creeping flow and the other one in the flow region:

$$Q^*=-\left(\underbrace{\int_0^{B_i}\dot{\gamma}_{rz}^*(r^*)r^{*2}dr^*}_{\text{yield stress zone}}+\int_{B_i}^1\dot{\gamma}_{rz}^*(r^*)r^{*2}dr^*\right)\cong-\int_{B_i}^1\dot{\gamma}_{rz}^*(r^*)r^{*2}dr^* \tag{36}$$

Upon substituting the shear strain (as a function of the Bingham number) into Eq. (36), the following expression for the volumetric flow with yield stresses is obtained:

$$Q^* = \varphi_\infty^*[B, \mathrm{B_i}]\frac{\sigma_{\mathrm{w}\infty}^*}{4} \Leftrightarrow Q^* = \mathrm{B_i}^{-1}\varphi_\infty^*[B, \mathrm{B_i}]\frac{\sigma_{\mathrm{y}}^*}{4}. \qquad (37a, b)$$

Equation (37b) is expressed in terms of the yield stress and the Bingham number, respectively, where the dimensionless fluidity of Eqs. (37a and b) has the following analytical form:

$$\varphi_\infty^*[B, \mathrm{B_i}] = \frac{1}{2B_{\mathrm{i}}^{-4}}\left\{\mathrm{B_i}^{-4} - 1 - 2\left(\mathrm{B_i}^{-2} - 1\right) + \left(\mathrm{B_i}^{-2} + 2B^{-1} - 1\right)\sqrt{\left(\mathrm{B_i}^{-2} - 1\right)^2 + 4B^{-1}\mathrm{B_i}^{-2}} - \left(2B^{-1}\right)^{3/2} + 4B^{-1}\left(B^{-1} - 1\right)\mathrm{Ln}\left|\frac{\mathrm{B_i}^{-2} + 2B^{-1} - 1 + \sqrt{\left(\mathrm{B_i}^{-2} - 1\right)^2 + 4B^{-1}\mathrm{B_i}^{-2}}}{2B^{-1} + 2\sqrt{B^{-1}}}\right|\right\} \qquad (38)$$

Note that the fluidity is used instead of the viscosity to avoid the situation where the viscosity tends to infinity. Equation (38) is the general yield stress fluidity function associated with the BMP constitutive equation. It is important to note that the dimensionless groups associated with the yield stress have the following asymptotic values:

$$B = \begin{cases} \dfrac{\eta_0}{\eta_\infty} = \dfrac{\varphi_\infty}{\varphi_0} \to \infty;\ B^{-1} = \dfrac{\eta_\infty}{\eta_0} = \dfrac{\varphi_0}{\varphi_\infty} \to 0;\ \to \mathrm{B_i} \to 1 \text{ (Hooke solid)} \\ \dfrac{\eta_0}{\eta_\infty} = \dfrac{\varphi_\infty}{\varphi_0} \to 1;\ B^{-1} = \dfrac{\eta_\infty}{\eta_0} = \dfrac{\varphi_0}{\varphi_\infty} \to 1;\ \to \mathrm{B_i} \to 0 \text{ (Newtonian fluid)} \end{cases}. \qquad (39)$$

The inverse of the dimensionless number B is related to a maximum number of structural points in the system and to the yield stress region. If the value of B (Eq. 47a) goes to infinity, its inverse tends to zero and the system does not flow ($\mathrm{B_i} = 1$), corresponding to the yield stress case. In contrast, when the inverse of the dimensionless B goes to one, the Bingham number tends to zero and its behavior is that of a viscous fluid ($\mathrm{B_i} = 0$). It is important to note that the dimensionless numbers (B^{-1}, $\mathrm{B_i}$) are not independent and satisfy the following linear relationship: $\mathrm{B_i}(B^{-1}) = 1 - B^{-1} \Leftrightarrow B^{-1}(\mathrm{B_i}) = 1 - \mathrm{B_i}$. The dimensionless fluidity (39) has the following asymptotic limit:

$$\varphi_\infty^*[B, \mathrm{B_i}] = \left\{ \lim_{\mathrm{B_i}\to 0} \varphi_\infty^*[B, \mathrm{B_i}] = 1;\ \lim_{\mathrm{B_i}\to 1} \varphi_\infty^*[B, \mathrm{B_i}] = 0 \lim_{B\to\infty} \varphi_\infty^*[B, \mathrm{B_i}] = \lim_{B^{-1}\to 0} \varphi_\infty^*[B, \mathrm{B_i}] = 1 - B_{\mathrm{i}}^4 \to 0, \mathrm{B_i} \to 1 \lim_{B\to 1} \varphi_\infty^*[B, \mathrm{B_i}] = \lim_{B^{-1}\to 1} \varphi_\infty^*[B, \mathrm{B_i}] = 1 \right. \qquad (40)$$

When the Bingham number goes to one, Eq. (40) represents the case of a Newtonian liquid, whereas the second equation is the case where the system presents the same structural points for any rate of deformation (Newtonian fluid), and the dimensionless fluidity is a fourth power of the Bingham number. In this case, the fluidity is one and zero for a Newtonian fluid and elastic solid, respectively (see Fig. 3)

First-order perturbation

Flow rate to first order

Shear thinning

The first order in the perturbation ε, namely $O(\varepsilon^1)$, renders $\sigma^{*1}(r^*, t^*) = \mathrm{n}(t^*)\sigma_0^*$, and the shear strain is given by the following expression:

$$\dot{\gamma}_1^*(r^*, t^*) = \left(\mathrm{n}(t^*) + \mathrm{We}_0\eta_0^*\dot{\mathrm{n}}(t^*)\right)\frac{\sigma_0^*}{\sigma_0^{*\cdot}};\ \dot{\sigma}_0^* \neq 0 \qquad (41)$$

Integrating Eq. (41), the axial velocity in terms of the material properties is obtained. However, we are interested in the perturbation solution of the flow rate. If the last expression is multiplied by the second power of the radial coordinate and further integrating the expression from zero to one, the flow rate equation is obtained:

$$Q_1^*\left[A_0, B, \sigma_{\mathrm{w}0}^*, t^*\right] = \varphi_1^*\left[A_0, B, \sigma_{\mathrm{w}0}^*, t^*\right]\frac{\sigma_{\mathrm{w}0}^*}{4} \qquad (42)$$

where the first dimensionless fluidity is given by the following expression:

$$\varphi_1^*\left[A_0, \mathrm{B}, \sigma_{\mathrm{w}0}^*, t^*\right] = \mathrm{n}\left(t^*\right)\varphi_{\mathrm{V}}^*\left[A_0, B, \sigma_{\mathrm{w}0}^*, t^*\right] + \dot{\mathrm{n}}\left(t^*\right)\mathrm{We}_0\,\varphi_{\mathrm{E}}^*\left[A_0, B, \sigma_{\mathrm{w}0}^*, t^*\right]. \qquad (43)$$

The viscous and elastic contributions are given by $\left\{\varphi_{\mathrm{V}}^*, \varphi_{\mathrm{E}}^*\right\}$

$$\varphi_{\mathrm{V}}^*\left[A_0, B, \sigma_{\mathrm{w}0}^*, t^*\right] = \frac{2}{\sigma_{\mathrm{w}0}^{*4}}\int_0^{\sigma_{\mathrm{w}0}^{*2}} \frac{\sigma_0^{*3}}{\sigma_0^{*\cdot}} d\sigma_0^*;\ \varphi_{\mathrm{E}}^*\left[A_0, B, \sigma_{\mathrm{w}0}^*, t^*\right] = \frac{2}{\sigma_{\mathrm{w}0}^{*4}}\int_0^{\gamma_{\mathrm{w}}^{*2}} \eta_0^{*4}\dot{\gamma}_0^{*2} d\dot{\gamma}_0^{*2}. \qquad (44a, b)$$

Taking the average of Eqs. (44a, b) and using the dimensionless stochastic function given in Eq. (18), the following analytical expression for the dimensionless pulsating fluidity to first order is obtained:

$$\left\langle \varphi_1^*(t^*)\right\rangle = 4\frac{dQ_0^*}{d\sigma_{w0}^*}\left\langle \mathrm{n}(t^*)\right\rangle = 4\frac{dQ_0^*}{d\sigma_{w0}^*}\left\langle \mathrm{n}(t^*)\right\rangle = \frac{dQ_0^*}{dQ_N^*}\left\langle \mathrm{n}(t^*)\right\rangle \quad (45)$$

Using the relationships of the dimensionless flow rate (see "Appendix" for the mathematical deduction of Eqs. 45 and 46)

$$\left\langle \varphi_1^*(t^*)\right\rangle = \left\langle \mathrm{n}(t^*)\right\rangle\left(1+\frac{d\mathrm{Ln}\varphi_0^*[A_0,B]}{d\mathrm{Ln}\sigma_{w0}^*}\right)\varphi_0^*[A_0,B] \quad (46)$$

Equations 45 and 46 are the expressions of the average fluidity to first order. It is important to note that the pulsating fluidity is determined by the derivative of the flow rate which is multiplied by the average of the stochastic function defined earlier. It can be calculated using the flow rate to first order (Eq. 42).

Yield stress

The analytical expressions should be scaled by the fluidity at high shear rate, since in the yield stress region the fluidity is equal to zero. Using Eq. (46) and proceeding as before, the average yield stress fluidity takes the following analytical form:

$$\left\langle \varphi_1^*(t^*)\right\rangle = 4\frac{dQ_0^*}{d\sigma_{w\infty}^*}\left\langle \mathrm{n}(t^*)\right\rangle \quad (47)$$

Applying the chain rule to Eq. (47), and following the same procedure as before, the following expression for the yield stress fluidity is obtained:

$$\left\langle \varphi_1^*(t^*)\right\rangle = \frac{dQ_0^*}{dQ_N^*}\left\langle \mathrm{n}(t^*)\right\rangle = \left(1+\frac{d\mathrm{Ln}\varphi_\infty^*[B,\mathrm{B_i}]}{d\mathrm{LnBi}^{-1}}\right)\varphi_\infty^*[B,\mathrm{B_i}]\left\langle \mathrm{n}(t^*)\right\rangle; Q_N^* = \frac{\sigma_y^{*-1}B_i^{-1}}{4} \quad (48)$$

Equation (48) has the same mathematical form of Eq. (46). The average volumetric flow can be expressed in the following reduced form:

$$\left\langle Q_1^*\left[A_0,B,\sigma_{w\infty}^*,t^*\right]\right\rangle = \sigma_y^{*-1}\frac{dQ_0^*}{dB_i^{-1}}\left\langle \mathrm{n}(t^*)\right\rangle \quad (49)$$

Flow rate calculation requires carrying out the inverse Bingham derivative of the yield stress flow rate of the BMP model through the analytical expression (Eqs. 37 and 28).

Fluidity enhancement

In particular, the fluidity enhancement can be calculated as the ratio of the fluidities to zeroth and first orders:

$$I_\varphi(\%) = \left(10\sqrt{\varepsilon}\right)^2\frac{\left\langle \varphi_1^*(A_x,B,t^*)\right\rangle}{\varphi_x^*(A_x,B)}; x=\{0,\infty\}. \quad (50)$$

In particular, for the shear thinning fluids, the fluidity enhancement can be expressed in terms of the flow rate enhancement, given by

$$I_Q(\%) = \left(10\sqrt{\varepsilon}\right)^2\frac{\left\langle Q_1^*(t^*)\right\rangle}{Q_0^*} = \left\langle \mathrm{n}(t^*)\right\rangle\left(10\sqrt{\varepsilon}\right)^2\left(1+\frac{d\mathrm{Ln}\varphi_0^*[A_0,B]}{d\mathrm{Ln}\sigma_{w0}^*}\right) \quad (51)$$

and for the yield stress, the fluidity enhancement is given by

$$I_{Qys}(\%) = \left(10\sqrt{\varepsilon}\right)^2\frac{\left\langle Q_1^*(t^*)\right\rangle}{Q_0^*} = \left\langle \mathrm{n}(t^*)\right\rangle\left(10\sqrt{\varepsilon}\right)^2\left(1+\frac{d\mathrm{Ln}\varphi_\infty^*[B,\mathrm{B_i}]}{d\mathrm{LnB_i^{-1}}}\right) \quad (52)$$

According to Eqs. (51–52) the shear-thinning fluidity enhancement is associated to the slope of the flow rate versus wall stress curve, whereas in the yield stress case, it is associated to the slope of the flow rate versus inverse of the Bingham number curve.

Local fluidity versus average fluidity

One way to compare the changes in fluidity to first order with respect to the zeroth order fluidity is through Eq. (1) associated to the flow enhancement. This ratio can be expressed as

$$I_\varphi(\%) = \left(10\sqrt{\varepsilon}\right)^2\left\langle \mathrm{n}(t^*)\right\rangle\frac{dQ_0^*\Big/dQ_N^*}{\int_0^{\sigma_{w0}^*}\varphi_0^*(A_0,B)d\sigma_{(rz)_0}^{*4}\Big/\int_0^{\sigma_{w0}^*}d\alpha} = I_0\frac{\text{local fluidity}}{\text{average fluidity}}. \quad (53)$$

According to this perturbation scheme, the flow enhancement is determined by the ratio of two fluidities. One of them is associated with the local changes of the dimensionless flow rate and the other one is associated with the dimensionless average fluidity. In Eq. (53), the flow enhancement I_0 is determined by ε and the amplitude of the perturbation in the stochastic function, i.e., $I_0 = \left(10\sqrt{\varepsilon}\right)^2\left\langle \mathrm{n}(t^*)\right\rangle$. In general,

the average fluidity can be expressed as an expansion in terms of a power series of the fluidity as follows:

$$\left\langle \varphi^*\left(A_0,B,t^*\right)\right\rangle = \left\langle Q^*\left(t^*\right)\Big/ Q_{\mathrm{N}}^*\right\rangle = \varepsilon^0\varphi_0^*(A_0,B) + \varepsilon^1\left\langle \varphi_1^*(A_0,B,t)\right\rangle + O\left(\varepsilon^2\right) \tag{54}$$

Notice that Eq. (54) is completely general and can be applied for any particular constitutive equation in the sense of the theory developed here. It then follows that the second-order dimensionless fluidity would be related to the convexity of the function associated with the dimensionless flow rate.

Time average energy

The non-dimensional work is defined as $W^*(t^*) = -2Q_0^*(t^*)\sigma_{\mathrm{w0}}^*(1+\varepsilon \mathrm{n}(t^*))$ (where Q_0 (t) is the flow rate) and $-2\sigma_{\mathrm{w0}}^*(1+\varepsilon \mathrm{n}(t^*))$ is the axial component of the pulsating pressure gradient. The fractional increase in energy I_{E} (%) is given by $I_{\mathrm{E}}(\%) = 100\ (<W^*(t^*)> - W_0^*)/W_0^*$, where $W_0^* = -2Q_0^*\sigma_{\mathrm{w0}}^*$ is the power required to pump the fluid without pulsations and $<W^*(t^*)>$ is the average power with pulsatile flow.

$$I_{\mathrm{E}}(\%) = 100\frac{\left\langle W^*(t^*)\right\rangle - W_0^*}{P_0^*} = 100\frac{\left\langle 2Q^*(t^*)\sigma_{\mathrm{w0}}^*(1+\varepsilon \mathrm{n}(t^*))\right\rangle - 2Q_0^*\sigma_{\mathrm{w0}}^*}{2Q_0^*\sigma_{\mathrm{w0}}^*} \tag{55}$$

Simplifying the last expression and splitting contributions to zeroth and first orders while the series given in Eqs. (23) is substituted into Eq. (55), the following expression is obtained:

$$I_{\mathrm{E}}(\%) = 100\varepsilon\frac{\left\langle Q_1^*(t^*)\right\rangle}{Q_0^*} + 100\varepsilon\left\langle \mathrm{n}\left(t^*\right)\right\rangle = I_{\mathrm{Q}}(\%) + I_0(\%) > 0 \tag{56}$$

The last expression is given by the sum of two contributions: (1) the energy associated to the flow enhancement I_{Q} (%) (Eqs. 1) and (2) a small energy I_0 (%) contribution related to the perturbation parameter and the average of the stochastic dimensionless function n (t^*). This means that the energy of the pumping fluid is always positive.

Pulsating energy and viscous energy (dissipated energy)

Since the flow enhancement caused by the pulsating pressure gradient represents an energetic advantage, we define a pulsating work as

$$\left\langle W_{\mathrm{pulsating}}^*\right\rangle = -\left\langle \varphi_1^*\left[A_0,B,\sigma_{\mathrm{w0}}^*,t^*\right]\right\rangle \sigma_{\mathrm{w0}}^{*2}\Big/2 \tag{57}$$

which should dominate over the fluid dissipation (viscosity). The total work associated with the pulse and the viscous mechanisms is given by the following mechanical balance:

$$\left(\Delta W^*\right)_{\mathrm{sist}} = \left\langle W_{\mathrm{pulsating}}^*\right\rangle - W_{\mathrm{viscous}}^* \tag{58}$$

Should an energetic advantage exist, the total work change must be zero, i.e., $(\Delta W^*)_{\mathrm{sist}} = 0$, and therefore the energy associated with the viscous mechanism would be the same of the pulsating energy:

$$W_{\mathrm{viscous}}^* = \left\langle W_{\mathrm{pulsating}}^*\right\rangle = -\left\langle \varphi_1^*\left[A_0,B,\sigma_{\mathrm{w0}}^*,t^*\right]\right\rangle = 8\frac{dQ_0^*}{dQ_{\mathrm{N}}^{-1}}\left\langle \mathrm{n}\left(t^*\right)\right\rangle \tag{59}$$

As demonstrated in the simulations (Figs. 9, 10, 11, 16, and 17), the effect of the pulsating pressure gradient is to decrease the irreversible work associated with the viscous dissipation. As a partial conclusion, this may be the reason by which some biological systems employ pulsating mechanisms to compensate the dissipation processes.

Results

Theoretical predictions

In this section, the simulations of the analytical results of the BMP constitutive equation for the case of pulsatile flow of blood at zero and first orders are presented.

Zeroth order theory

Shear-thinning and shear-thickening mechanisms

At low shear strain, the fluidity is constant (first Newtonian region) for all cases and coincides with the Newtonian curve (see Fig. 4, case c). The system is highly structured, and the value of the dimensionless number B is equal to unity. The response is independent of the ratio between the structural relaxation time and the viscoelastic flow. At a critical value of the dimensionless wall stress, the fluidity increases monotonically, attaining a constant value at a second critical wall stress (second Newtonian region corresponding to a structure aligned completely to the flow direction, see Fig. 4 cases a and b). The value of the dimensionless numbers

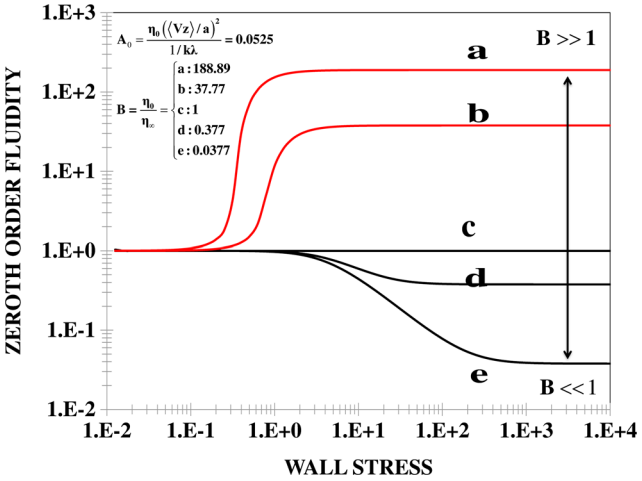

Fig. 4 Dimensionless fluidity as a function of the dimensionless wall stress for shear- thinning and shear-thickening conditions varying B for fixed A_0. Numerical values of the BMP parameters and dimensionless numbers are given in Tables 1 and 2

$\{A_0, B\}$ employed in the simulation are displayed in Table 2. For the cases d and e in Fig. 4, the system attains a highly structured state, displaying a monotonically increasing power-law region with a slope close to unity at moderate wall stresses, followed by a constant value at high wall stress (second Newtonian zone). The values of the dimensionless numbers $\{A_0, B\}$ are always less than one and larger than one, respectively ($A_0 << 1$, $B >> 1$). It is important to note that, for zero order, no flow enhancement is predicted. The following predictions (Figs. 4, 5, 6, and 7) correspond entirely to the unperturbed steady simple shear flow with a constant pressure gradient.

Figure 5 shows the flow rate as a function of the wall stress for different shear thinning and thickening conditions as the number B varies.

At a critical dimensionless wall stress, the flow rate increases sharply from a Newtonian reference curve (constant slope curve) to a power-law region of continuous increasing slope behavior (Fig. 5, curves a and b). In the case of the shear-thickening fluids (curves d and e), the system departs from the Newtonian curve displaying smaller flow rates with a power-law tendency. It is important to note that the flow rate is a function of the physical interactions associated with the structure of a complex fluid, and for the case of blood, the aggregation–disaggregation mechanism of blood cells caused by flow is reflected through the A_0 and B numbers.

Thixotropy

Figure 6a, b shows the fluidity (a) and viscosity (b), for several values of A_0 (which accounts for the ratio of kinetics of rupture to the structure time) and B (ratio of Newtonian viscosities, at low and high shear rate). In Fig. 6a, all curves show an initial constant fluidity (first Newtonian zone) and at a critical wall stress, the fluidity increases sharply followed by a second constant fluidity (second Newtonian region). Upon increasing A_0, the critical transition is shifted to lower wall stresses. Figure 6b shows the corresponding curves of flow rate versus wall stress.

To analyze the effect of the thixotropy and rheopexy (Figs. 5a, b, 6a, b), the value of the kinetic constant is changed to $k = G_0^{-1}$, enabling A_0 to be the ratio $A_0 = \left(\eta_0 G_0^{-1}\right)/\lambda$ when

Table 2 Magnitude of the dimensionless numbers

Dimensionless numbers	$A_0 = \frac{k\lambda\eta_0}{t_c^2}$	$A_\infty = \frac{k\lambda\eta_\infty}{t_c^2}$	$B = \frac{\eta_0}{\eta_\infty}$	$A_0 = \frac{\lambda\lambda_0}{t_c^2}$; $k = G_0^{-1}$	$A_\infty = \frac{\lambda\lambda_\infty}{t_c^2}$; $k = G_0^{-1}$
Shear thickening	0.13727	0.00518	26.5		
		0.0518	2.65		
Shear thinning	5.18	25.9	0.2		
Newtonian	0.13727	0.13727	1		
Yield stress	0.00259	271.95	9.52×10^{-6}		
	0.0259		9.52×10^{-6}		
	0.13727		5.04×10^{-6}		
	25.9		0.0952381		
	271.95		1		
Thixotropy			185	9.85×10^{-1}	1
			18.5	9.85×10^{-2}	10
			1.85	9.85×10^{-3}	50
			0.185	9.85×10^{-4}	100

Characteristic time $t_c = a/\langle V\rangle \cong \lambda$. In wormlike micellar systems: $k = 1/G_0$

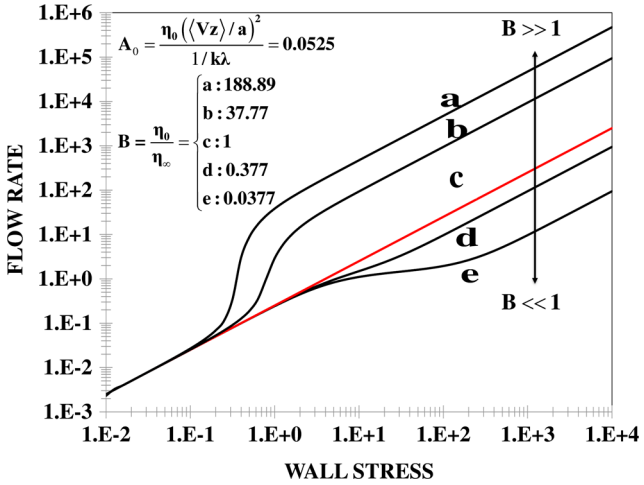

Fig. 5 Dimensionless flow rate as a function of the dimensionless wall stress for shear-thinning and shear-thickening conditions varying B for fixed A_0. Values of the BMP parameters and dimensionless numbers are given in Tables 1 and 2

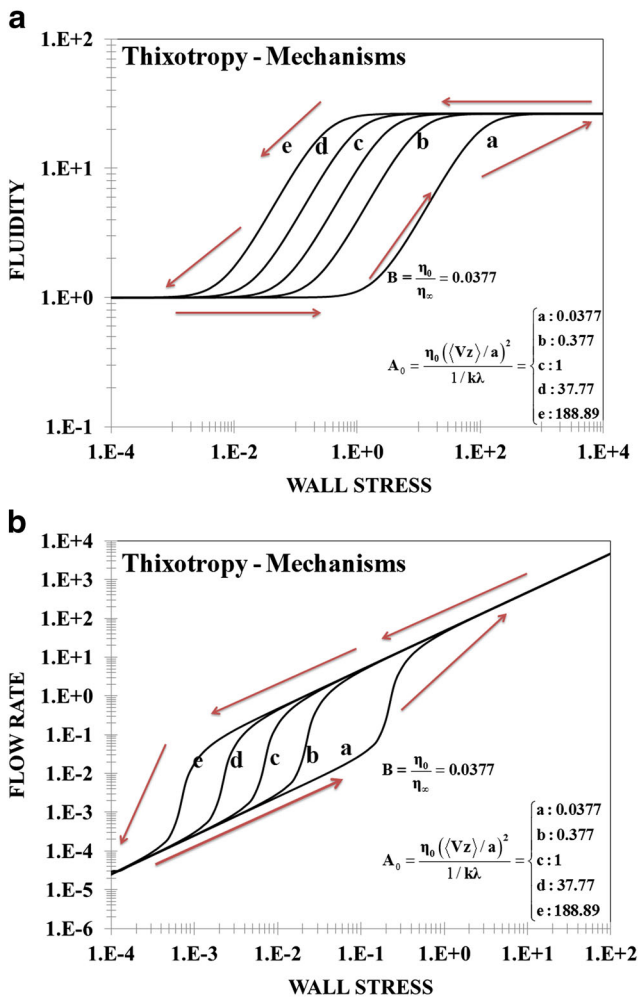

Fig. 6 **a** Zero-order fluidity as functions of A_0 for shear-thinning conditions (B = 0.0377). Values of the BMP parameters and dimensionless numbers are given in Tables 1 and 2. **b** Flow rate as functions of A_0 for shear-thinning conditions (B = 0.0377). Values of the BMP parameters and dimensionless numbers are given in Tables 1 and 2

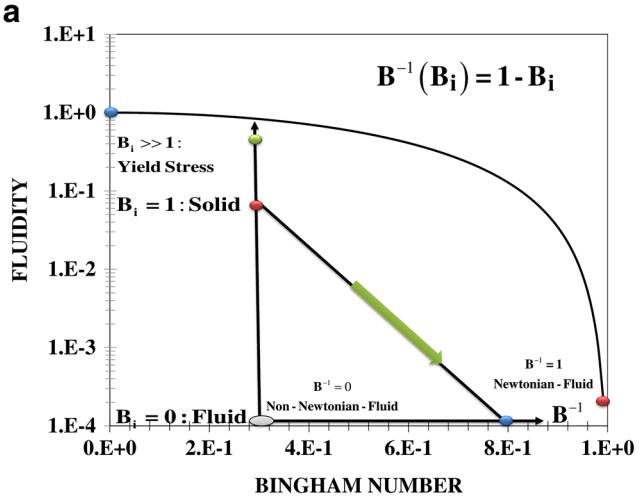

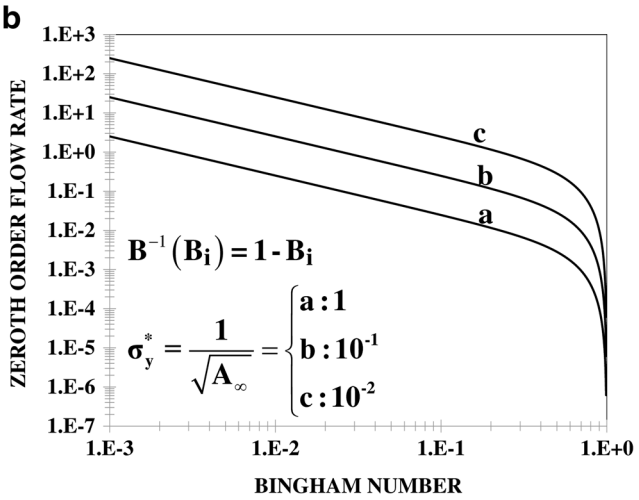

Fig. 7 Fluidity (**a**) and flow rate (**b**) versus Bingham number. **a** The *inset* shows a map with different cases of the Bingham number. **b** The effect of the yield stress for the shear thickening case is shown. BMP parameters and dimensionless numbers are given in Tables 1 and 2

$\lambda = t_c$. When the value of A_0 lies in the range $A_0 \in (0, 1) \subset R$, the structure does not recover during the deformation period. In contrast, when the value of A lies in the range $1 \leq A_0 = (\eta_0 G_0^{-1}) / \lambda$, the structure recovers rapidly by the effect of the flow. It is important to note that the shape of the thixotropic and rheopexy loops is determined exclusively by the value of A_0.

Yield stress mechanisms

In Fig. 7, the fluidity (Fig. 7a) and flow rate (Fig. 7b) are plotted with the Bingham number. For low values of the Bingham number (B_i < <1), the fluidity is equal to one (Newtonian region). When the Bingham increases, the fluidity decreases (tending asymptotically to zero) as B_i tends to one, since the system is near the yield stress (elastic solid state). In Fig. 7b, for small Bingham numbers (B_i < <1) the flow rate

decreases as a power-law (constant slope), while at a critical Bingham number, the flow rate tends to zero abruptly.

Pulsatile shear thinning mechanism

First order theory

Figure 8 shows model predictions of the fluidity versus wall stress for various values of B (which relates the zero shear-rate viscosity to the maximum shear-rate viscosity). Curves 8a and 8b correspond to a shear thinning fluid with $B > 1$. Curve c corresponds to the Newtonian fluid ($B = 1$) and curves d and e correspond to the shear thickening fluid ($B < 1$). The effect of the pulsations can be observed in the maxima in the fluidity displayed by the shear-thinning fluid at intermediate shear rates (curves a and b) and the minima displayed by the shear-thickening fluid (curves d and e). The Newtonian fluid is unaffected by the pulsations. The pulsatile flow has a flow enhancement effect on the system by increasing the fluidity (viscosity reduction) in the region where the fluid becomes shear thinning. Thereafter, this effect disappears as the second Newtonian region is approached at high shear rates. In the case of the shear thickening fluid, the opposite effect is observed, where minima appears at the onset for shear thickening and vanishes as the second Newtonian region is approached. To our understanding, this is the first time that the flow enhancement is explained in terms of an increase in the fluidity which leads to an increase in the flow rate. This mechanism may be associated with the optimum pumping work of the heart associated with a variable pressure gradient, implying an optimized process of energy consumption.

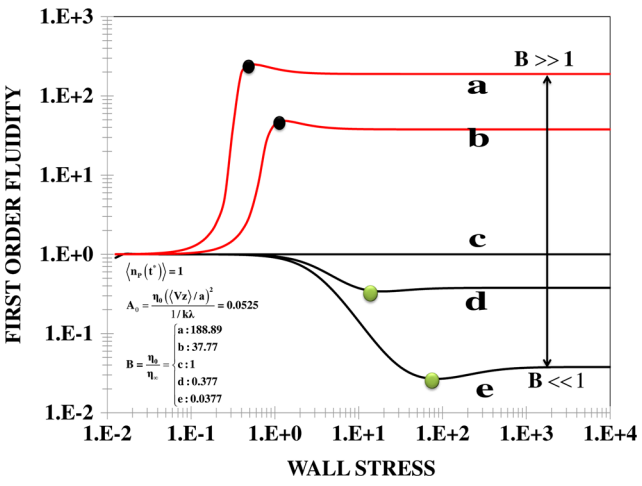

Fig. 8 Pulsating fluidity as a function of the wall stress for various shear-thinning (*a*, *b*) and shear thickening (*d*, *e*) conditions corresponding to different values of the parameter B. The BMP parameters and dimensionless numbers are given in Tables 1 and 2

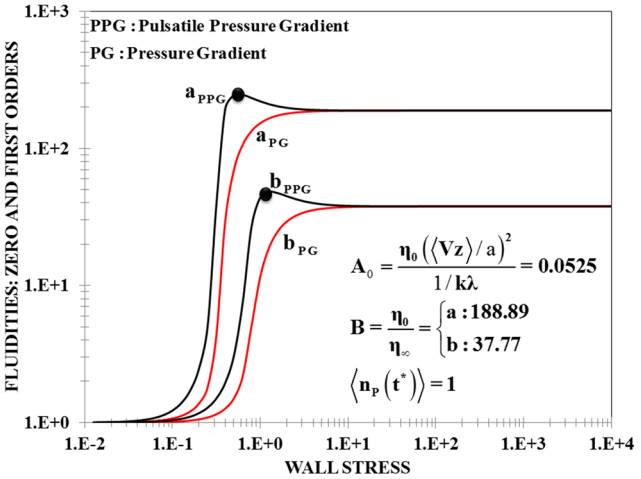

Fig. 9 Pulsating fluidity as a function of the wall stress for various shear-thinning conditions. The BMP parameters and dimensionless numbers are given in Tables 1 and 2

Since the blood behaves as a shear thinning fluid, this case will be examined in detail. In Fig. 9, the fluidity versus wall stress for a shear thinning fluid is plotted. The case of the constant pressure gradient (zero order, PG) is compared to the case of the pulsatile pressure gradient (first order prediction, PPG). The former displays a smooth transition from the constant fluidity at low wall stress values to that corresponding to the second Newtonian region.

To clearly expose effect of shear thinning upon the magnitude of the flow enhancement, Fig. 10 depicts the flow rate variation with wall stress for two shear thinning cases.

Curves in Fig. 11 shows a maximum flow enhancement in the region where the fluid exhibits shear thinning (power law

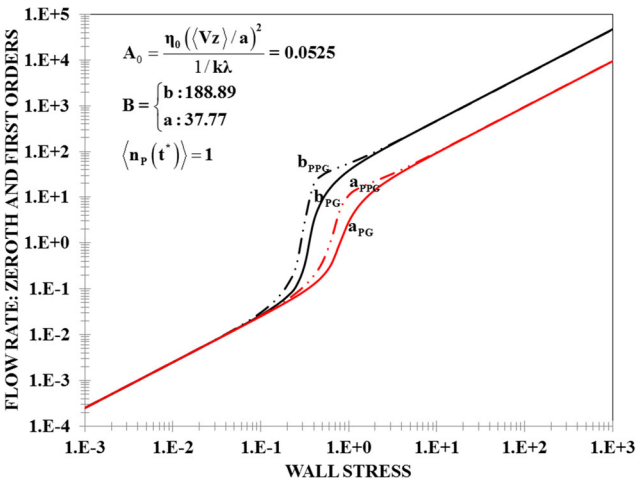

Fig. 10 Fluidity enhancement versus wall stress for various shear-thinning fluids. BMP parameters and dimensionless numbers are given in Tables 1 and 2

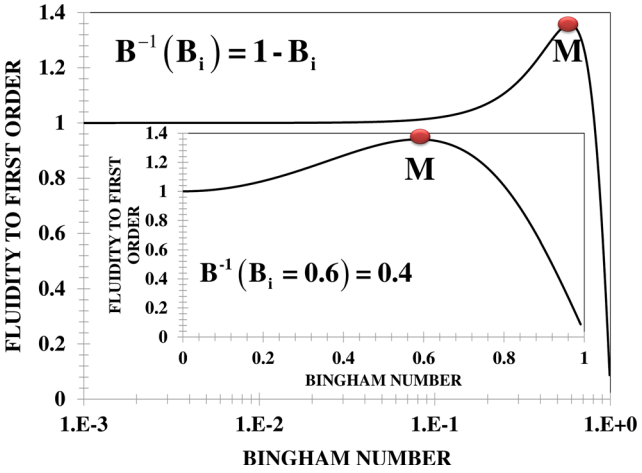

Fig. 11 Fluidity enhancement versus wall stress for two shear-thinning fluids. BMP parameters and dimensionless numbers are given in Tables 1 and 2

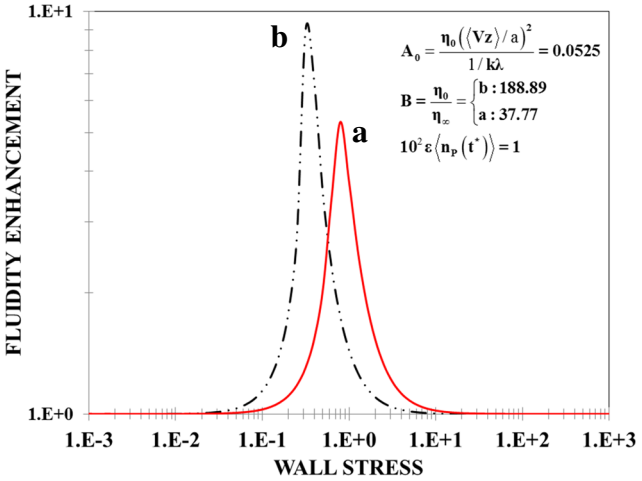

Fig. 13 Fluidity enhancement versus wall stress for a shear-thinning fluid. The parameters used in the simulation are given in Tables 1 and 2

region). In the regions of low and high wall stresses (corresponding to Newtonian viscosities at low and high shear rate), the fluid exhibits no flow enhancement. The value of the maximum is dependent on the strength of shear thinning, with the highest value corresponding to the fluid with strongest shear thinning.

Yield stress mechanisms

Figure 12 shows the flow rate as a function of the Bingham number for the first order approximation (dotted line). In this case, there is an increase in the flow rate at high values of the Bingham number which is caused by the pulsations, since without pulsations (continuous line), no increase is observed (see Fig. 4 cases a and b). The effect of the pulse is evident only in the region near the yield stress ($B_i = 1$). The maximum is higher depending on the strength of shear thinning.

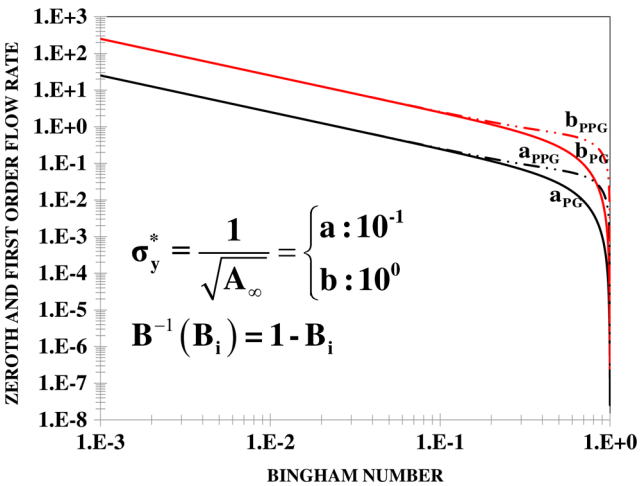

Fig. 12 Flow rate versus Bingham number for two yield-stress fluids. The parameters used in the simulation are given in Tables 1 and 2

Figure 13 shows the fluidity enhancement as a function of the wall stress. The effect of B (ratio of the zero shear-rate viscosity to the infinity shear-rate viscosity) is to shift the maximum fluidity enhancement to the left. This number also controls the magnitude of the fluidity enhancement since it is a measure of the strength of the shear-thinning mechanisms.

Predictions of the fluidity enhancement using data for blood with different cholesterol levels

In this section, the fluidity enhancement is predicted in real human blood data with low, intermediate, and high cholesterol levels. To give a brief description, reversible changes in the structure that may occur at low shear rates are neglected. Material parameters are given in Tables 3 (BMP model parameters) and 4 (rheometric data). Parameters in Table 3 were fitted with an algorithm programmed in Mathematica 10.

Typical blood radius of veins varies from 0.02 to 0.35 cm and the density of the blood is approximately 1.05 g/cm^3, respectively (Del Rio et al. 1998). The characteristic dimensionless shear rate can be calculated from rheometric data:

$$0.085\ \mathrm{s}^{-1} = \frac{\langle V\rangle}{a_{\max}} = \left(\dot{\gamma}_{\mathrm{car}}\right)_{\min} \le \dot{\gamma}_{\mathrm{car}} \le \left(\dot{\gamma}_{\mathrm{car}}\right)_{\max} = \frac{\langle V\rangle}{a_{\min}} = 1.5\ \mathrm{s}^{-1}$$

The ratio of inertial and viscous forces can be calculated through the Reynolds number, i.e.,

$$0.0051 = \frac{\rho\langle V\rangle a_{\min}}{\eta_0} = \mathrm{Re}_{\min} \le \mathrm{Re} \le \mathrm{Re}_{\max} = \frac{\rho\langle V\rangle a_{\max}}{\eta_0} = 0.191$$

Since the Reynolds number is less than unity, inertia is small.

Table 3 Material parameters values of the BMP equation

Material properties	Kinetic constant k $[Pa^{-1}]$	Restructuration time λ [s]	Elastic moduli G_0 [Pa]	Viscosity at low shear rate η_0 [Pas]	Viscosity at high shear rate η_∞ [Pas]
Low cholesterol 114 mg/dL	0.90	0.810	1. 487	0.0113	0.009
Medium cholesterol 174 mg/dL	0.74	1	1.472	0.023	0.0042
High cholesterol 300 mg/dL	0.19	0.884	1.834	0.046	0.0047

Figure 14 shows the BMP predictions intended to fit the low shear rate region of the viscosity curves with various cholesterol levels. Only one mode of the model is employed with parameters shown in Table 3. As reported by Moreno et al. (2015), three modes are necessary to fit the whole range of data up the high shear rate zone. The main mode describes the data along the low and moderate shear regions, where the yield stress arises. Blood fluidities predictions for real human blood are depicted in Fig. 15, where the solid line represents the zero-order approximation (no flow enhancement) and the dotted line represents the first-order predictions. As the cholesterol content increases, the fluidity increase is more evident since cholesterol induces stronger shear thinning.

The comparison of the fluidity enhancement maxima for blood with different cholesterol levels is depicted in Fig. 16. The inset in Fig. 16 shows the results for the energy enhancement which are directly related to the fluidity enhancement as defined in Eq. (72). As the cholesterol content increases, the energy enhancement maxima is larger, evidencing that for this particular solution, an energetic advantage of the pumping work exists (optimization of the pumping work by compensating the viscous dissipation of the fluid) under oscillating conditions.

Results of flow rate are depicted in Fig. 17 where the largest increase in flow rate is observed in the sample with high cholesterol content. Again, the increase in flow rate is observed only in the shear-thinning region of the fluid (power-law region). In the low and high wall stress regions, corresponding to the Newtonian plateaus, no difference is observed between the constant pressure gradient and pulsatile pressure gradient cases.

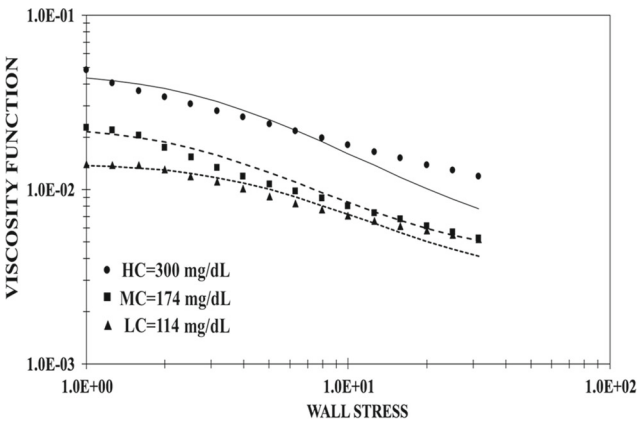

Fig. 14 Rheometric flow data of blood with different cholesterol contents. *Continuous lines* show predictions of the BMP model, using the parameters shown in Table 3

Conclusions

In this work, a perturbation solution to a pulsating pressure gradient flow of blood using the BMP constitutive equation is analyzed for a general class of pressure gradient noises, comparing results for the zero and first order approximations. The following conclusions are summarized:

(a) The fluidity enhancement predicted by the BMP model can be separated into two contributions: viscous and viscoelastic, where both are function of the amplitude of the pulsating pressure gradients and the dimensionless parameters associated to the shear thinning and yield stress mechanisms.
(b) The fluidity enhancement is determined by a ratio of a local fluidity and an average integral fluidity.
(c) A necessary condition to obtain a fluidity enhancement in a structured fluid is that the fluid undergoes transitions

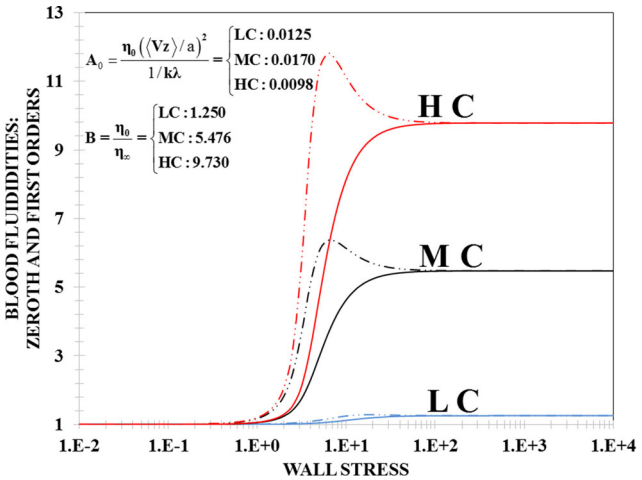

Fig. 15 Fluidity versus wall stress for shear thinning fluids. *L*, *M*, and *H* correspond to cholesterol content (low, medium, high). *Solid lines* correspond to the zero order fluidity (no flow enhancement), and *discontinuous lines* correspond to the first-order solutions of the fluidity (flow enhancement). Parameters and dimensionless numbers used in the simulation are given in Tables 3 and 4

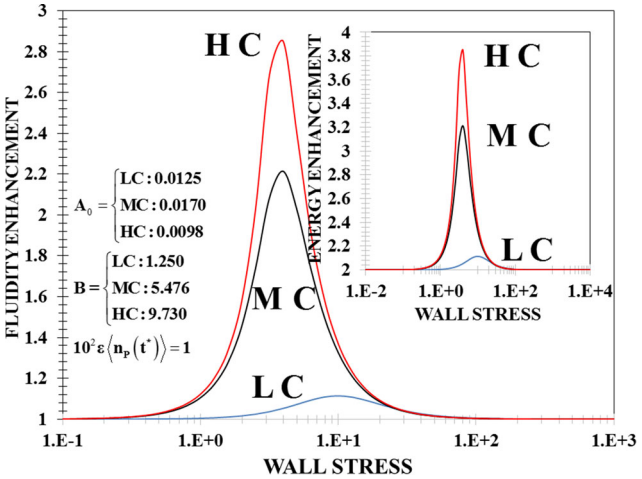

Fig. 16 Fluidity enhancement versus wall stress for blood with different cholesterol content: *LC* low, *MC* medium, and *HC* high cholesterol content. The parameters and dimensionless numbers used in the simulation are given in Tables 2 and 3

from a high-structured state to a less structured one induced by flow, namely, $B = \eta_0/\eta_\infty >> 1$. The flow curve must contain a power-law zone.

(d) The viscoelastic, kinetic, and structural mechanisms in the BMP model were characterized by dimensionless groups assigned to each mechanism.

(e) In a biological liquid, thixotropy can be interpreted as a particular case of the rupture and structural mechanisms in the fluid, namely, $A_0 = \lambda\lambda_0(\langle Vz\rangle/a)^2$, where the kinetic constant is the normalized constant for the shear stress, i.e., $k = G_0^{-1}$.

(f) The fluidity enhancement was found to be directly related to the concentration of cholesterol in blood samples, with the sample with high cholesterol content showing the largest values of the fluidity enhancement.

(g) The yield stress to zero order shows a constant behavior when the Bingham number tends to zero (Newtonian Fluid) and a complex solid behavior when the Bingham number is close to one.

(h) The yield stress is predicted to be controlled by two dimensionless numbers $\{B_i, B^{-1}\}$, which are related to the shear thinning and thickening processes through the fluidities ratio. Both dimensionless numbers are linearly linked.

(i) The effect of the pulsating pressure is seen at the transition from low to high-structured states, i.e., when the Bingham number is close to one.

The non-linear model presented here is only valid for a pressure gradient noise of sufficiently small amplitude. For the particular solution presented here, there is an energetic advantage of the pumping work, which is optimized by a fluidity enhancement caused by the oscillating pressure gradient, which compensates the viscous dissipation of the fluid. This effect is directly related to the cholesterol content of blood.

Future work

It would be worthwhile to compare the theoretical predictions of the effect of the kinetic, viscoelastic, and rupture mechanisms by using human blood with different human pathologies such as (1) diabetic blood, (2) anemic blood, and (3) umbilical cord blood (Bureau et al. 1979, 1980).

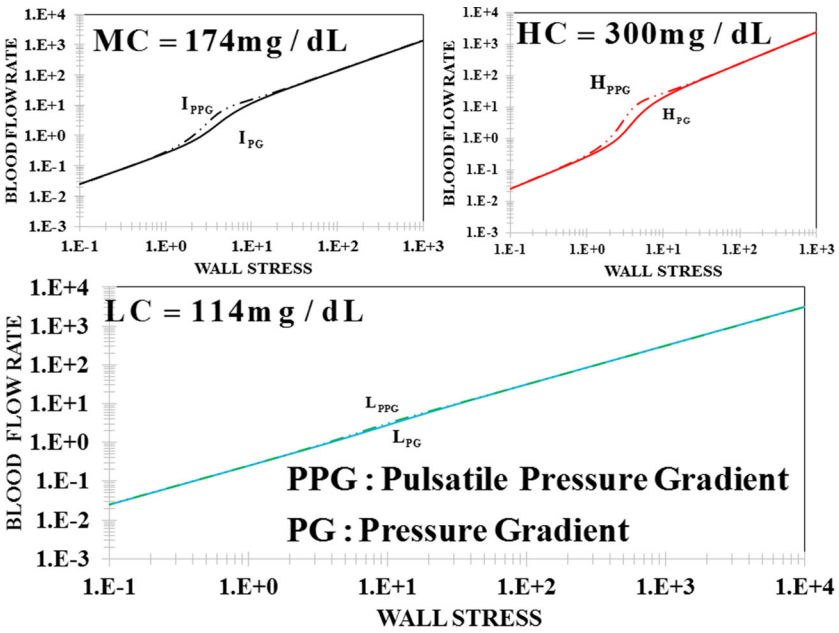

Fig. 17 Flow rate as a function of wall stress for various fluids with varying cholesterol content. The parameters and dimensionless numbers are given in Tables 2 and 3

Table 4 Dimensionless numbers obtained from rheometric blood data

Dimensionless numbers	$A_0 = \frac{k\lambda\eta_0}{t_c^2}$	$A_\infty = \frac{k\lambda\eta_\infty}{t_c^2}$	$B = \frac{\eta_0}{\eta_\infty}$	$\mathrm{We}_0 = \frac{\eta_0}{G_0 t_c^{-1}}$	$\sigma_y^* = 1/\sqrt{A_\infty}$
Low cholesterol 114 mg/dL	0.0125	0.010	1.250	0.0061	10.0
Medium cholesterol 174 mg/dL	0.0170	0.0031	5.476	0.0156	17.94
High cholesterol 300 mg/dL	0.0098	0.0010	9.703	0.0222	31.47

Characteristic time $t_c = a/< V > \cong \lambda$

Analysis of the combined pulsating and oscillating flow on the fluidity functions coupled with viscous dissipation in complex flows deserves further analysis.

Extension of these rheological equations in the linear and non-linear oscillatory flow with the contributions of Fourier formalism (higher harmonics) is an important issue that deserves future research on pulsating flow.

Finally, this work aims to model pulsating biological flows (blood with cholesterol). Further investigations should deal with other relevant flow conditions (elongation, oscillatory flows, and flow instabilities) to fully describe a realistic blood flow system.

Acknowledgments EEHV gratefully acknowledges financial support from projects IN115615 and PE112716, respectively.

Appendix
Derivation of the flow rate using the BMP fluid in a cylindrical tube

In this appendix, the overall calculation of the flow rate is presented. Substitution of the shear strain to zero order in the equation for the flow rate, the following expression is obtained:

$$Q_0^* = \frac{1}{2A_0\sigma_{w0}^*}\int_0^1 \left(A_0 B\left(\sigma_{w0}^* r^*\right)^2 - 1 + \sqrt{\left(A_0 B\left(\sigma_{w0}^* r^*\right)^2 - 1\right)^2 + 4A_0\left(\sigma_{w0}^* r^*\right)^2}\right) r^* dr^* \tag{60}$$

Upon a change of variables $U = A_0\left(\sigma_{w0}^* r^*\right)^2$; $r^* dr^* = dU/2A_0\sigma_{w0}^{*2}$, the flow rate is given by the expression

$$\begin{aligned} Q_0^* &= \frac{1}{4A_0^2\sigma_{w0}^{*3}}\int_0^{A_0\sigma_{w0}^{*2}} \left(BU - 1 + \sqrt{(BU-1)^2 + 4U}\right) dU \\ &= \frac{1}{4A_0^2\sigma_w^{*3}}\left(\frac{A_0^2 B}{2}\sigma_{w0}^{*4} - A_0^2\sigma_{w0}^{*2} + BI\right), \end{aligned} \tag{61}$$

solving the previous integral:

$$I = \int_0^{A_0\sigma_{w0}^{*2}} \left(\sqrt{(U-\varphi_B)^2 + 4\,\varphi_B^2 U}\right) dU. \tag{62}$$

The integral kernel can be changed in the same form as for the axial velocity:

$$\begin{aligned} &\sqrt{(U-\varphi_B)^2 + 4\varphi_B^2 U} \\ &\quad = \sqrt{U^2 + 2\varphi_B(2\varphi_B - 1)U + (\varphi_B(2\varphi_B - 1))^2 + \varphi_B^2 - (\varphi_B(2\varphi_B - 1))^2} \end{aligned} \tag{63}$$

The constants are given by

$$\begin{aligned} &\delta_1^2 = \varphi_B^2 - (\varphi_B(2\varphi_B - 1))^2 = (\varphi_B + \varphi_B(2\varphi_B - 1))(\varphi_B - \varphi_B(2\varphi_B - 1)) = 4\varphi_B^3(1-\varphi_B) \\ &\delta^2 = (\varphi_B(2\varphi_B - 1))^2; \delta_1^2 + \delta^2 = \varphi_B^2 \end{aligned} \tag{64}$$

Substituting the previous definitions into the integral, and applying the same change of variables in the integral, i.e., $U + \delta = \delta_1 \tan\theta$; $dU = \delta_1 \sec^2\theta$, we obtain

$$\begin{aligned} I &= \int_0^{A_0\sigma_{w0}^{*2}} \left(\sqrt{(U+\delta)^2 + \delta_1^2}\right) dU = \delta_1^2 \int_0^{A_0\sigma_{w0}^{*2}} \sec^3\theta d\theta \\ &= \frac{1}{2}\left(\sec\theta\tan\theta + \mathrm{Ln}|\sec\theta + \tan\theta|\right) \end{aligned} \tag{65}$$

The last integral can be calculated directly using a partial cyclical integration, according to the following variable change: $U = \sec\theta$; $dV = \sec^2\theta d\theta$, and the result is inserted in the general expression of the volumetric flow rate (Eq. 61). Upon changing the U variable in terms of the dimensionless numbers and wall stress, the analytical volumetric flow rate is obtained as a function of the dimensionless numbers discussed previously (Eqs. 25a and 31). It is important to mention that the control variable is the flow rate and gives rise to a non-linear algebraic equation $\Omega : R^3 \to R^1$; $\Omega\left[A_0, B, \sigma_{w0}^*\right] = Q_{BMP}^*\left[A_0, B, \sigma_{w0}^*\right] - Q_N^* \times \varphi_0^*\left[A_0, B, \sigma_{w0}^*\right]$. Given the numbers $\{A_0, B\}$ from the rheometric data and the flow rate $Q\left[A_0, B, \sigma_{w0}^*\right]$, the pressure gradient can be calculated using a standard iterative produce such as Newton–Raphson:

$$p_0^* - p_L^* = \int_0^{L^*} \sigma_{w0}^* dz^* = -\frac{1}{2}\int_0^{L^*} \nabla^* p^* dz^*. \tag{66}$$

References

Acierno A, La Mantia FP, Marrucci G, Titomanlio G (1976) A non linear viscoelastic model with structure dependent relaxation times. I Basic formulation J Non-Newton Fluid Mech 1:125–146

Anand M, Rajagopal KR (2004) A shear-thinning viscoelastic fluid model for describing the flow of blood. Int J Cardiovasc Med Sci 4:59–68

Anand M, Kwack J, Masud A (2013) A new generalized Oldroyd-B model for blood flow in complex geometries. Int J Eng Sci 72:78–88

Apostoldis AJ, Moyer AP, Beris AN (2016) Non-Newtonian effects in simulations of coronary arterial blood flow. J Non-Newton Fluid Mech 233:155–165

Apostolidis AJ, Beris AN (2015) The effect of cholesterol and triglycerides on the steady state rheology of blood. Rheol Acta 1:1–13

Barnes HA, Towsend P, Walters K (1969) Flow of non-Newtonian liquids under a varying pressure gradient. Nature 224:585–587

Barnes HA, Towsend P, Walters K (1971) On pulsatile flow of non-Newtonian liquids. Rheol Acta 10:517–527

Bautista F, Soltero JFA, Pérez-López JH, Puig JE, Manero O (2000) On the shear banding flow of elongated micellar solutions. J Non-Newton Fluid Mech 94:57–66

Bautista F, De Santos JM, Puig JE, Manero O (1999) Understanding thixotropic and antithixotropic behavior of viscoelastic micellar solutions and liquid crystalline dispersions. The model J Non-Newton Fluid Mech 80:93–113

Bautista F, Soltero JFA, Macias ER, Manero O (2002) On the shear banding flow of wormlike micelles. J Phys Chem B 106:13018–13026

Bautista F, PérezLópez JH, García JP, Puig JE, Manero O (2007) Stability analysis of shear banding flow with the BMP model. J NonNewtonian Fluid Mech, 144:160–169

Brust M, Schaefer C, Doerr R, Pan L, Garcia M, Arratia P, Wagner C (2013) Rheology of human blood plasma: viscoelastic versus Newtonian behavior. Phys Rev Lett 110:078305

Bureau M, Healy JC, Bourgoin D, Joly M (1979) Etude rhéologique en régime transitoire de quelques échantillons de sangs humains artificiellement modifies. Rheol Acta 18:756–768

Bureau M, Healy JC, Bourgoin D, Joly M (1980) Rheological hysteresis of blood at low shear rate. Biorheology 17:191–203

Calderas F, Sánchez-Solis A, Maciel A, Manero O (2009) The transient flow of the PETPEN-Montmorillonite clay nanocomposite. Macromol Symp Macromex 283-284:354–360

Calderas F, Herrera-Valencia EE, Sanchez-Solis A, Manero O, Medina-Torres L, Renteria A, Sanchez-Olivares G (2013) On the yield stress of complex materials. Korea-Aust Rheol J 25:233–242

Caram Y, Bautista F, Puig JE, Manero O (2006) On the rheological modeling of associative polymers. Rheol Acta 56:45–57

Chen J, Lu X (2006) Numerical investigation of the non-Newtonian pulsatile blood flow in a bifurcation model with a non-planar branch. J Biomech 39:818–832

Davies JM, Bhumiratana S, Bird RB (1978) Elastic and inertial effects in pulsatile flow of polymeric liquids in circular tubes. J Non-Newtonian Fluid Mech 3:237–259

De Andrade Lima LRP, Rey AD (2005) Pulsatile Poiseuille flow of discotic mesophases. Chem Eng Sci 60:6622–6636

De Andrade Lima LRP, Rey AD (2006) Pulsatile flows of Leslie-Ericksen liquid crystals. J Non-Newton Fluid Mech 135:32–45

De Kee D, Chan Man Fong CF (1994) Rheological properties of structured fluids. Polym Eng Sci 34:438–445

Del Rio JA, López de Haro M, Whitaker S (1998) Enhancement in the dynamic response of a viscoelastic fluid flowing in a tube. Phys Rev E 58:6323–6327

EL-Shahed M (2003) Pulsatile flow of blood through a stenosed porous medium under periodic body acceleration. Appl Math Comput 138: 479–488

Escalante JI, Escobar D, Macias ER, Perez-Lopez JH, Bautista F, Mendizabal E, Puig JE, Manero O (2007) Effect of a hydrotope on the viscoelastic properties of polymer-like micellar solutions. Rheol Acta 46:685–691

Fredrickson AG (1964) Principles and applications of rheology. Prentice-Hall, Englewood Cliffs

Ghasemi SE, Hatami M, Hatami J, Sahebi SAR, Ganji DD (2016) An efficient approach to study the pulsatile blood flow in femoral and coronary arteries by Differential Quadrature Method. Physica A 443:406–414

Giesekus H (1966) Die Elastizitat von Flussigkeiten. Rheol Acta 5:29–35

Giesekus H (1982) A simple constitutive equation for polymer fluids based on the concept of deformation-dependent tensorial mobility. J Non-Newtonian Fluid Mech 11:69–109

Giesekus H (1984) On configuration-dependent generalized Oldroyd derivatives. J Non-Newtonian Fluid Mech 14:47–65

Giesekus H (1985) Constitutive equation for polymer fluids based on the concept of configuration dependent molecular mobility: a generalized mean-configuration model. J Non-Newtonian Fluid Mech 17: 349–372

Herrera EE, Calderas F, Chavez AE, Manero O, Mena B (2009) Effect of random longitudinal vibration on the Poiseuille flow of a complex liquid. Rheol Acta 48:779–800

Herrera-Valencia EE, Calderas F, Chávez AE, Manero O (2010) Study on the pulsating flow of a worm-like micellar solution. J Non-Newtonian Fluid Mech 165:174–183

Kolbasov A, Comiskey PM, Sahu RP, Sinha-Ray S, Yarin AL, Sikarwar BS, Kim S, Jubery TZ, Attinger D (2016) Blood rheology in shear and uniaxial elongation. Rheol Acta 55:901–908

Lin Y, Han Tan GW, Phan-Thien N, Cheong Khoo B (2015) Flow enhancement in pulsating flow of non-colloidal suspension in tubes. J Non-Newtonian Fluid Mech 202:13–17

Macıas ER, Bautista F, Soltero JFA, Puig JE, Attane P, Manero O (2003) On the shear thickening flow of dilute CTAT wormlike micellar solutions. J Rheol 47:643–658

Majhi SN, Nair VR (1994) Pulsatile flow of third grade fluids under body acceleration-modelling blood flow. Internat J Eng Sci 32:839–846

Manero O, Mena B (1977) An interesting effect in non-Newtonian flow in oscillating pipes. Rheol Acta 19:277–284

Manero O, Walters K (1980) On elastic effects in unsteady pipe flows. Rheol Acta 19:277–284

Manero O, Bautista F, Soltero JFA, Puig JE (2002) Dynamics of worm-like micelles: the Cox-Merz rule. J Non-Newtonian Fluid Mech 106: 1–15

Manero O, Pérez-López JH, Escalante JI, Puig JE, Bautista F (2007) A thermodynamic approach to rheology of complex fluids: the generalized BMP model. J Non-Newton Fluid Mech 146:22–29

Massoudi M, Phuoc TX (2008) Pulsatile flow of blood using a modified second-grade fluid model. Comput Math Appl 56:199–211

Mena B, Manero O, Binding DM (1979) Complex flow of viscoelastic fluids through oscillating pipes. Interesting effects and applications J Non-Newtonian Fluid Mech 5:427–448

Moreno L, Calderas F, Sanchez-Olivares G, Medina-Torres L, Sanchez-Solis A, Manero O (2015) Effect of cholesterol and triglycerides levels on the rheological behavior of human blood. Korea-Aust Rheol J 27:1–10

Moyers-Gonzalez MA, Owens RG (2010) Mathematical modelling of the cell-depleted peripheral layer in the steady flow of blood in a tube. Biorheology 47:39–71

Moyers-Gonzalez MA, Owens RG, Fang J (2008a) A nonhomogeneous constitutive model for human blood: part 1. Model derivation and steady flow. J Fluid Mech 617:327–354

Moyers-Gonzalez MA, Owens RG, Fang J (2008b) A nonhomogeneous constitutive model for human blood: part II. Asymptotic solution for large Péclet numbers. J Non-Newtonian Fluid Mech 155:146–160

Moyers-Gonzalez MA, Owens RG, Fang J (2008c) A nonhomogeneous constitutive model for human blood: part III. Oscillatory flow. J Fluid Mech 155:161–173

Nandakumar N, Sahu KC, Anand M (2015) Pulsatile flow of a shear-thinning model for blood through a two-dimensional stenosed channel. Eur J Mech B-Fluid 49:29–35

Owens RG (2006) A new micro structure-based constitutive model for human blood. J Non-Newtonian Fluid Mech 140:57–70

Owens RG, MoyersGonzalez M, Fang J (2008) On the simulation of steady and oscillatory blood flow in a tube using a new nonhomogeneous constitutive model. Biorheology 45:83–84

Phan-Thien N (1978) On pulsating flow of polymeric fluids. J Non-Newtonian Fluid Mech 4:167–176

Phan-Thien N (1980a) Flow enhancement mechanism of a pulsating flow of non-Newtonian liquids. Rheol Acta 19:285–290

Phan-Thien N (1980b) The effects of longitudinal vibration on pipe flow of a non-Newtonian fluid. Rheol Acta 19:539–547

Phan-Thien N (1981) On pulsating flow of a polymer fluids: strain-dependent memory kernels. J Rheol 25:293–314

Phan-Thien N (1982) On a pulsating flow of slightly non-Newtonian liquids. J Méc Théo Appl 1:81–89

Phan-Thien N, Dudek J (1982a) Pulsating flow of a plastic fluid. Nature 296:843–884

Phan-Thien N, Dudek J (1982b) Pulsating flow revisited. J Non-Newton Fluid-Mech 11:147–161

Prakash J, Ogulu A (2007) A study of pulsatile blood flow modeled as a power law fluid in a constricted tube. Int Commun Heat Mass Transfer 34:762–768

Quemada D (1981) A rheological model for studying the hematocrit dependence of red cell-red cell and red cellprotein interactions in blood. Biorheology 18:501–516

Rao LVM (2014) $sPLA_2$-V: A new player in thrombosis? J Thromb Haemost 12:1918–1920

Razavi A, Shirani E, Sadeghi MR (2011) Numerical simulation of blood pulsatile flow in a stenosed carotid artery using different rheological models. J Biomech 44:2021–2030

Reddy JVR, Srikanth D, Murthy SVSSNVGK (2014) Mathematical modelling of pulsatile flow of blood through catheterized unsymmetric stenosed artery—effects of tapering angle and slip velocity. Eur J Mech B-Fluid 48:236–244

Siddiqui SU, Verma NK, NMishra S, Gupta RS (2009) Mathematical modelling of pulsatile flow of Casson's fluid in arterial stenosis. App Math and Comp 210:1–10

Soltero JFA, Puig JE, Manero O (1999) Rheology of cetyltrimethylammonium p-toluenesulfonate-water system. 3. Nonlinear viscoelasticity. Langmuir 15:1604–1612

Sousa PC, Carneiro J, Pinho FT, Oliveira MSN, Alves MA (2013) Steady and large-oscillatory shear rheology of whole blood. Biorheology 50:269–282

Sousa PC, Pinho FT, Alves MA, Oliveira MSN (2016) A review of hemorheology: measuring techniques and recent advances. Korea-Aust Rheol J 28:1–22

Sun N, Kee DD (2001) Simple shear, hysteresis and yield stress in biofluids. Can J Chem Eng 79:36–41

Tabatabaei S, López-Aguilar JE, Tamaddon-Jahromi HR et al (2015) Rheol Acta 54:869–885

Tian F, Zhu L, Fok P, Lu X (2013) Simulation of a pulsatile non-Newtonian flow past a stenosed 2D artery with atherosclerosis. Comput Biol Med 43:1098–1113

Tropea C, Yarin AL, Foss JF (2007) Springer handbook of experimental fluid mechanics, volume 1. Springer Science and Busines Media, Berlin